computation

MDPI

Article

Effect of Heated Wall Corrugation on Thermal Performance in an L-Shaped Vented Cavity Crossed by Metal Foam Saturated with Copper–Water Nanofluid

Luma F. Ali [1,*], Hussein Togun [2] and Abdellatif M. Sadeq [3,*]

[1] Mechanical Engineering Department, College of Engineering, University of Baghdad, Baghdad 10071, Iraq
[2] Thi-Qar Technical College, Southern Technical University, Basrah 61001, Iraq; hussein-tokan@stu.edu.iq
[3] Department of Mechanical and Industrial Engineering, College of Engineering, Qatar University, Doha P.O. Box 2713, Qatar
* Correspondence: luma.f@coeng.uobaghdad.edu.iq (L.F.A.); as1004958@qu.edu.qa (A.M.S.)

Abstract

Practical applications such as solar power energy systems, electronic cooling, and the convective drying of vented enclosures require continuous developments to enhance fluid and heat flow. Numerous studies have investigated the enhancement of heat transfer in L-formed vented cavities by inserting heat-generating components, filling the cavity with nanofluids, providing an inner rotating cylinder and a phase-change packed system, etc. Contemporary work has examined the thermal performance of L-shaped porous vented enclosures, which can be augmented by using metal foam, using nanofluids as a saturated fluid, and increasing the wall surface area by corrugating the cavity's heating wall. These features are not discussed in published articles, and their exploration can be considered a novelty point in this work. In this study, a vented cavity was occupied by a copper metal foam with $PPI = 10$ and saturated with a copper–water nanofluid. The cavity walls were well insulated except for the left wall, which was kept at a hot isothermal temperature and was either non-corrugated or corrugated with rectangular waves. The Darcy–Brinkman–Forchheimer model and local thermal non-equilibrium models were adopted in momentum and energy-governing equations and solved numerically by utilizing commercial software. The influences of various effective parameters, including the Reynolds number ($20 \leq Re \leq 1000$), the nanoparticle volume fraction ($0\% \leq \varphi \leq 20\%$), the inflow and outflow vent aspect ratios ($0.1 \leq D/H \leq 0.4$), the rectangular wave corrugation number ($N = 5$ and $N = 10$), and the corrugation dimension ratio ($CR = 1$ and $CR = 0.5$) were determined. The results indicate that the flow field and heat transfer were affected mainly by variations in Re, D/H, and φ for a non-corrugated left wall; they were additionally influenced by N and CR when the wall was corrugated. The fluid- and solid-phase temperatures of the metal foam increased with an increase in Re and D/H. The fluid-phase Nusselt number near the hot left sidewall increased with an increase in φ by $(25–60)\%$, while the solid-phase Nusselt number decreased by $(10–30)\%$, and these numbers rose by around 3.5 times when the Reynolds number increased from 20 to 1000. For the corrugated hot wall, the Nusselt numbers of the two metal foam phases increased with an increase in Re and decreased with an increase in D/H, CR, or N by 10%, 19%, and 37%. The original aspect of this study is its use of a thermal, non-equilibrium, nanofluid-saturated metal foam in a corrugated L-shaped vented cavity. We aimed to investigate the thermal performance of this system in order to reinforce the viability of applying this material in thermal engineering systems.

check for updates

Academic Editor: Gamal Ismail

Received: 19 July 2025
Revised: 26 August 2025
Accepted: 29 August 2025
Published: 6 September 2025

Citation: Ali, L.F.; Togun, H.; Sadeq, A.M. Effect of Heated Wall Corrugation on Thermal Performance in an L-Shaped Vented Cavity Crossed by Metal Foam Saturated with Copper–Water Nanofluid. *Computation* **2025**, *13*, 218. https://doi.org/10.3390/computation13090218

Copyright: © 2025 by the authors. Licensee MDPI, Basel, Switzerland. This article is an open access article distributed under the terms and conditions of the Creative Commons Attribution (CC BY) license (https://creativecommons.org/licenses/by/4.0/).

Keywords: convection; L-shaped; vented cavity; metal foam; nanofluid; corrugated; non-corrugated; thermal performance

1. Introduction

Convective heat transfer in cavities has attracted a great deal of interest from both the scientific and engineering communities due to its use in many applications, such as in heat exchangers, electronic cooling, chemical processing, solar applications, the thermal management of batteries, and many more. Some applications require the presence of ventilation ports in enclosures, such as for air conditioning, convective drying, the ventilation of buildings, and many others [1–3]. Additionally, some uses require porous media to improve convection heat transmission [4–9]. Different enclosure shapes have been researched in the literature, including L-shaped cavities [10–17]. This type of cavity has been studied by many researchers, some of whom have filled these enclosed L-shaped cavities with porous media saturated with pure water or nanofluids. Natural convection heat transfer in L-shaped porous enclosures was explored numerically in ref. [18] for different parameter values of Darcy (*Da*) and Rayleigh (*Ra*) numbers and different inclination angles. The researchers noticed that an inclination angle with a high *Ra* number affected the streamlines and temperature contours. The authors of ref. [19] scrutinized an L-shaped porous cavity with a moving top wall and different parameter values for the *Re*, Grashof (*Gr*), and *Da* numbers. They deduced that the average fluid temperature decreases by up to 8% with higher *Da* and *Gr* numbers. The influence of radiation and an external electric field on a lid-driven porous cavity was analyzed by utilizing the finite element method to examine the effect on the *Re* and *Da* numbers, φ, and the supplied voltage. This problem was handled in ref. [20], and the authors deduced that the convective mode is enhanced with an increasing *Da* number and radiation parameter. Moreover, the author of ref. [21] studied natural convection in a closed L-configuration enclosure equipped with layers of porous media to improve the rate of heat transfer. Several parameters were kept constant, including the location of the porous layers, the location and shape of the heating blocks located on the cavity walls, the *Da* and *Ra* numbers, and the enclosure inclination angle. The utilization of porous layers intensified the convection heat transfer rate for higher *Ra* numbers. Additionally, heat transfer through convection in an L-shaped enclosure filled with aluminum–water-saturated metal foam was considered in ref. [22], and the effect of the aspect ratio, the container tilting angle, the Hartmann number, and the porosity was investigated. The authors determined that the cooling rate is enhanced and entropy generation is decreased; in addition, there was no influence of the container tilt angle or the magnetohydrodynamic properties on the thermal performance inside the cavity. The authors of ref. [23] numerically explored the unsteady mixed convection characteristics in an L-shaped porous lid-driven cavity saturated with different volume fractions of solid particles in a nanofluid. Various values of the *Da*, *Re*, and Richardson (*Ri*) numbers were also investigated, and the authors found that the *Re* and *Da* numbers had considerable influence on the thermal behavior. Furthermore, by employing both a response surface methodology and a computational analysis, the authors of ref. [24] achieved the greatest possible natural convection in an irregular L-shaped cavity occupied with porous media. They explored the effect of the aspect ratio and the *Da* number on the thermal behavior in the cavity, and found that there was an improvement in the *Nu* number and a decline in the magnitude of the surface temperature and entropy when the aspect ratio and *Da* number were increased.

Vented enclosures occupied with porous media saturated with water or a nanofluid have been considered by many researchers, including enclosures with different shapes, different boundary conditions, different inlet and outlet port widths and locations, different numbers of inlet and outlet vents, and many other conditions, such as the magnetohydrodynamic presence, the type of porous media (metal foam), and so on. The topic of a mixed convection flow in ventilated cavities filled with fluid-saturated porous media was investigated numerically and experimentally in refs. [25–33]. The authors studied many variations of the *Ra*, *Da*, and *Re* numbers; the porosity; different outlet port positions; and the inlet and outlet port width. Generally, they concluded that the *Nu* number increases with an increasing inlet/outlet opening width and higher *Ra*, *Da*, and *Re* numbers; the overall transfer of heat in the cavity was influenced by the width of the vents and the outlet port's position, and the heat and flow field characteristics were dependent on a medium porosity. In addition, the authors found that the presence of porous media inside the vented cavity generally strengthened the convection heat transfer and improved the thermal performance. On the other hand, several researchers have examined enclosures filled with porous media saturated with a nanofluid. The authors of refs. [34–37] investigated this type of problem for various values of *Ra*, *Da*, and *Re* numbers; nanoparticle concentrations; inclination angles; amplitudes of the cavity's wavy wall; and dimensions of the input and output portions. Universally, heat transfer was enhanced by higher *Ra* and *Re* numbers, larger sizes of the inlet/outlet sections, an increased wavy amplitude cavity, and a higher nanoparticle volume fraction. In general, an aiding flow is more effective for the *Nu* number matched with the opposing circumstance.

In addition, cavities with inlet and outlet ports may be crossed by a nanofluid only. These types of enclosures have been investigated by numerous researchers, including the authors of refs. [38–43]. These investigators examined the influence of varying the *Re* and *Ri* numbers, φ, the aspect ratio of the cavity, the modes of imposed external flows (injection and suction), the inclination angle, and the locations of the inlet and outlet ports. As a result of their work, they determined that the transfer of heat characteristics increases with an increase in the *Ri* and *Re* numbers and φ, and a reduction in the average bulk temperature occurs when the solid concentration in the nanofluid is increased.

Very few studies were found in the literature that have investigated L-shaped open cavities, either the vented type or the channel type, irrespective of the fluid or material used to fill the cavity. Unsteady hydromagnetic mixed convection for an L-shaped open cavity channel supplied with a porous inner layer and heat-generating components was carried out numerically in refs. [44,45]. The authors examined the effect of the porous layer thickness; the size of the heat-generating components; the *Da*, *Re*, *Gr*, and Hartmann numbers; the porosity; the orientation of the magnetic field; and φ on the fluid field and the transferring heat characteristics. Their results mainly revealed that an increase in the thickness of the porous layer, the *Re* number, or the nanoparticle concentration enhanced the overall thermal performance. Additionally, the authors of refs. [46,47] achieved the numerical generation of entropy and mixed-convection heat transfer in an L-shaped inclined channel filled with a Ag–water nanofluid. The outcome of varying the *Re* number, *Ri* number, aspect ratio, inclination angle, aspect ratio, and volume fraction of solid nanoparticles was examined in these studies. Accordingly, the results demonstrated that both the *Ri* and *Re* numbers enhanced the mean *Nu* number and minimized the rate of generation of entropy. The same result was achieved when the aspect ratio was increased. Meanwhile, the rate of entropy generation and the *Nu* number increased when the nanoparticle volume fraction was increased. For the same shape of channel, the authors of ref. [48] accomplished the turbulent transport of a hybrid commixture, comprising copper nanoparticles and aluminum oxide, to analyze the generation of heat characteristics via forced convection.

They studied the outcome of changing both the volume of the nanoparticles and the *Re* number and deduced that, at the middle of the channel, the *Nu* number was augmented by increasing the volume fractions; in addition, the transport of a hybrid mixture is more beneficial when the *Re* number is high.

Furthermore, a numerical study of mixed convection within an L-shaped vented enclosure furnished by a nanofluid beneath a magnetic field effect was investigated in ref. [49]. The parameters implemented in this study included the Hartmann and *Re* numbers and φ. The authors presumed that the nanofluid enhanced the heat transfer performance and an increasing *Re* number strengthened the hydrodynamic field and developed the transfer of heat, specifically in cases where the magnetic field was absent. Meanwhile, the authors of ref. [50] numerically assessed the magnetohydrodynamic convection of a hybrid nanofluid and the change in the phase process inside an L-configuration vented enclosure provided with an inner rotating cylinder and a phase-change packed system. Their study implemented various values of *Re*, rotational *Re*, the Hartmann number, and the cylinder size. Varying the rotating cylinder size and its rotational speed can be used to control the size of vortices and their distribution within the cavity.

Continuous developments in vented cavities are being investigated in order to enhance the heat and fluid flow. These developments can be accomplished through altering relevant parameters, the medium within the enclosure, and the inlet and outlet dimensions and positions, or by choosing a suitable shape for these cavities according to the relevant engineering application. According to a literature survey and author knowledge, a vented L-shaped cavity filled with porous media has not been studied previously, despite the fact that it has wide applications in convective drying, thermal management, electronic cooling, and solar collectors. Moreover, previous studies that have researched this type of cavity have failed to investigate many important points, including the use of a metal foam with a local thermal non-equilibrium and saturated with nanofluids of different volume fraction concentrations; the effect of wall corrugation on the heat transfer performance; varying dimensions of the inlet and outlet vents; etc. Therefore, the authors of this study considered a vented L-shaped cavity packed with a copper–water nanofluid-saturated copper metal foam in order to examine the above points. Such a system can be employed in many applications, including solar air heating, in order to enhance the heat transmission rate, and this represents a new topic within this field. Another important novelty of this paper is the presence of a cavity vertical wall corrugation and the investigation of the effect of the corrugation number and size on the thermal performance. It is known that wall corrugation results in a heat transfer enhancement by increasing the contact surface area with the saturated porous media. The obtained results were confirmed with a good agreement.

2. Computational Methods

2.1. Problem Statement and Boundary Conditions

This study considered a steady, two-dimensional, L-shaped, vented enclosure with a non-corrugated or corrugated left wall comprising copper metal foam saturated with copper nanoparticles submerged in water. The left vertical sidewall of the cavity was kept at an isotherm hot temperature, T_h, whereas the remaining walls were well insulated. A physical model of the problem is illustrated in Figure 1, which shows the L-shaped enclosure with an equal height H and length L, a slot at the left upper edge for the cold fluid T_c inlet, and a vent in the top right corner for fluid outflow. Additionally, two cases were considered in the current study for the left sidewall, as depicted in Figure 1b: non-corrugated and corrugated. The temperature difference of the left wall and the stream temperature of a constant velocity u_c at the cavity inlet indicated that the buoyancy influences through the inflow and outflow vents of width D were responsible for producing the forced convection.

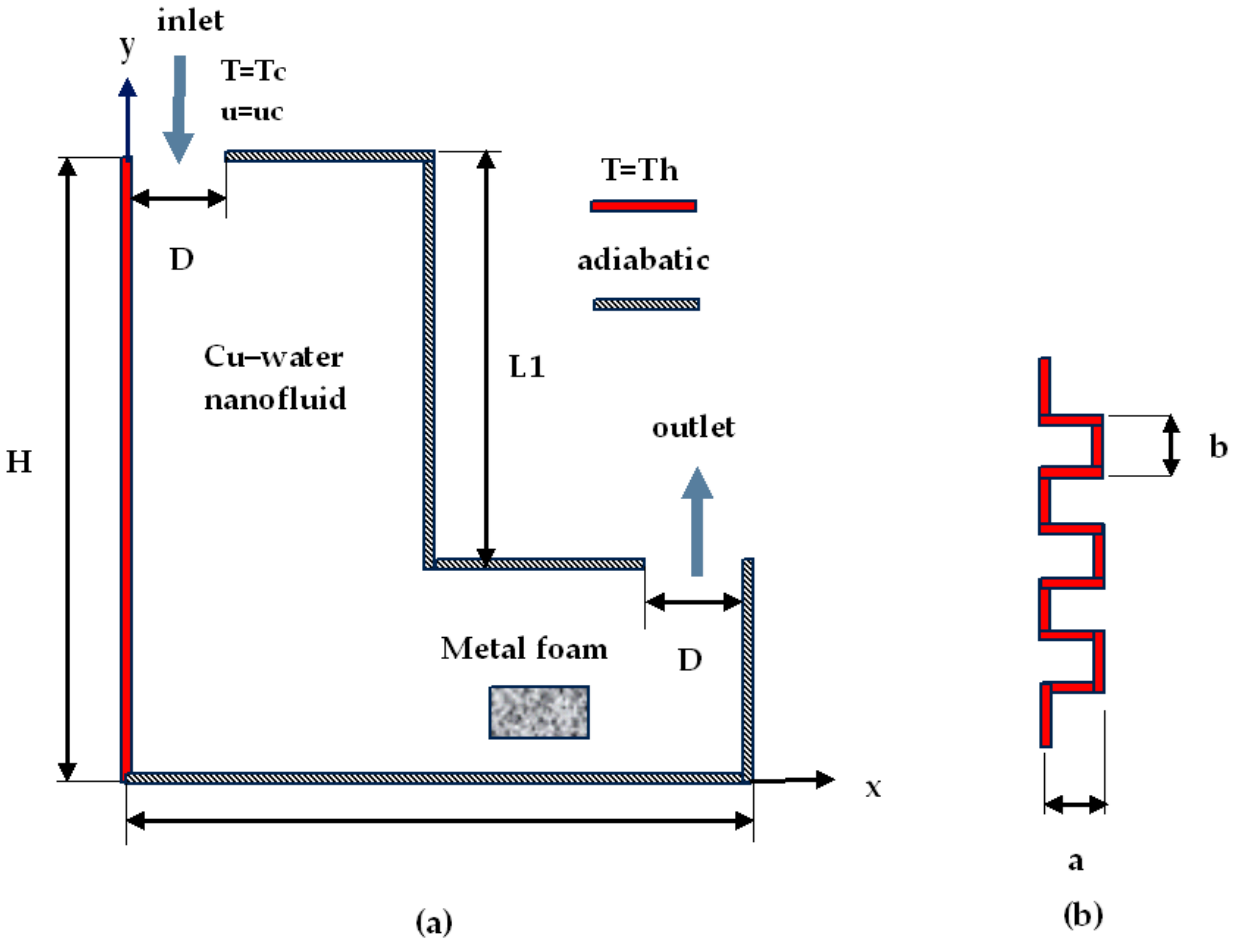


Figure 1. Physical diagram of L-shaped vented enclosure with non-corrugated or corrugated left vertical sidewall: (**a**) schematic of physical domain; (**b**) corrugation dimension of left sidewall.

2.2. Computational Formations and Assumptions

This study assumed that the present model had a steady state, was incompressible, and exhibited laminar flow, and the heat transmission rate through radiation and the effects of viscous dissipation were presumed to be insignificant. In addition, it was assumed that the porous medium was hydrodynamically and thermally isotropic, homogeneous, and saturated with a single-phase nanofluid in a local thermal non-equilibrium with the metal foam solid phase. It was also assumed that the base fluid (water) and the solid nanoparticles (copper) were in a thermal equilibrium and that there was no slip velocity between them. The model utilized for the porous medium was the Darcy–Brinkman–Forchheimer model. According to all the mentioned assumptions, the governing equations can be written as follows [23,51]:

Continuity equation:

$$\frac{\partial u}{\partial x} + \frac{\partial v}{\partial y} = 0, \tag{1}$$

Momentum equations:

$$\frac{1}{\varepsilon^2}\left(\rho_{nf} u \frac{\partial u}{\partial x} + \rho_{nf} v \frac{\partial u}{\partial y}\right) = -\frac{\partial p}{\partial x} + \frac{\mu_{nf}}{\varepsilon}\left(\frac{\partial^2 u}{\partial x^2} + \frac{\partial^2 u}{\partial y^2}\right) - \frac{\mu_{nf}}{K} u - \frac{C_F \rho_{nf}}{K^{1/2}} u\sqrt{u^2 + v^2}, \tag{2}$$

$$\begin{aligned}\frac{1}{\varepsilon^2}\left(\rho_{nf} u \frac{\partial v}{\partial x} + \rho_{nf} v \frac{\partial v}{\partial y}\right) &= -\frac{\partial p}{\partial y} + \frac{\mu_{nf}}{\varepsilon}\left(\frac{\partial^2 v}{\partial x^2} + \frac{\partial^2 v}{\partial y^2}\right) - \frac{\mu_{nf}}{K} v - \frac{C_F \rho_{nf}}{K^{1/2}} v\sqrt{u^2 + v^2} + \\ &\quad (\rho\beta)_{nf} g\left(T_{nf} - T_c\right),\end{aligned} \tag{3}$$

where C_F is the Forchheimer coefficient, which can be calculated from $C_F = \frac{1.75}{\sqrt{150\varepsilon^3}}$ [52].

Energy equations:

$$\left(\rho C_p\right)_{nf}\left[u\frac{\partial T_{nf}}{\partial x} + v\frac{\partial T_{nf}}{\partial y}\right] = \varepsilon k_{nf}\left[\frac{\partial^2 T_{nf}}{\partial x^2} + \frac{\partial^2 T_{nf}}{\partial y^2}\right] + h_{sf}a_{sf}\left(T_s - T_{nf}\right), \tag{4}$$

$$(1-\varepsilon)k_s\left[\frac{\partial^2 T_s}{\partial x^2} + \frac{\partial^2 T_s}{\partial y^2}\right] + h_{sf}a_{sf}\left(T_{nf} - T_s\right) = 0, \tag{5}$$

For this study, the metal foam characteristics (for instance, the interfacial area density (a_{sf}), the permeability, the interfacial heat transfer coefficient (h_{sf}), and additional specifications, along with the porous material properties) can be found in refs. [53–55].

The below non-dimensional numbers and specifications were integrated to reformulate governing equations into a non-dimensional structure with the purpose of generalizing the work and lessening the inspection parameters:

$X = \frac{x}{H}$, $Y = \frac{y}{H}$, $U = \frac{u}{u_c}$, $V = \frac{v}{u_c}$, $P = \frac{p}{\rho_{nf}u_c^2}$, $Re = \frac{\rho_f u_c H}{\mu_f}$, $Da = \frac{K}{H^2}$, $\theta_{nf} = \frac{T_{nf}-T_c}{T_h-T_c}$, $Gr = \frac{g\beta(T_h-T_c)\rho_f^2 H^3}{\mu_f^2}$, $\theta_s = \frac{T_s-T_c}{T_h-T_c}$, $Pr = \frac{\mu_f C_f}{k_f}$, $\alpha_f = \frac{k_f}{\rho_f C p_f}$, $Nu_{fs} = \frac{h_{sf}a_{sf}H^2}{k_f}$, $\alpha_{nf} = \frac{k_{nf}}{\left(\rho C_p\right)_{nf}}$.

Consequently, Equations (1)–(5) can be presented as follows:

Continuity equation:

$$\frac{\partial U}{\partial X} + \frac{\partial V}{\partial Y} = 0, \tag{6}$$

Momentum equations:

$$U\frac{\partial U}{\partial X} + V\frac{\partial U}{\partial Y} = -\varepsilon^2\frac{\partial P}{\partial X} + \frac{\rho_f}{\rho_{nf}}\frac{\mu_{nf}}{\mu_f}\frac{\varepsilon}{Re}\left(\frac{\partial^2 U}{\partial X^2} + \frac{\partial^2 U}{\partial Y^2}\right) - \frac{\varepsilon^2}{ReDa}\frac{\rho_f}{\rho_{nf}}\frac{\mu_{nf}}{\mu_f}U - \frac{\varepsilon^2 C_F}{Da^{1/2}}U\sqrt{U^2+V^2}, \tag{7}$$

$$U\frac{\partial V}{\partial X} + V\frac{\partial V}{\partial Y} = -\varepsilon^2\frac{\partial P}{\partial Y} + \frac{\varepsilon}{Re}\frac{\mu_{nf}}{\mu_f}\frac{\rho_f}{\rho_{nf}}\left(\frac{\partial^2 V}{\partial X^2} + \frac{\partial^2 V}{\partial Y^2}\right) - \frac{\varepsilon^2}{ReDa}\frac{\mu_{nf}}{\mu_f}\frac{\rho_f}{\rho_{nf}}V - \frac{\varepsilon^2 C_F}{Da^{1/2}}V\sqrt{U^2+V^2} + \frac{\varepsilon^2 Gr}{Re^2}\frac{(\rho\beta)_{nf}}{\rho_f\beta_f}\theta_{nf}, \tag{8}$$

Energy equations:

$$U\frac{\partial\theta_{nf}}{\partial X} + V\frac{\partial\theta_{nf}}{\partial Y} = \frac{\alpha_{nf}}{\alpha_f}\frac{\varepsilon}{RePr}\left[\frac{\partial^2\theta_{nf}}{\partial X^2} + \frac{\partial^2\theta_{nf}}{\partial Y^2}\right] + \frac{Nu_{fs}}{RePr}\frac{\rho_f Cp_f}{\left(\rho C_p\right)_{nf}}\left(\theta_s - \theta_{nf}\right), \tag{9}$$

$$\frac{(1-\varepsilon)k_s}{k_{nf}}\left[\frac{\partial^2\theta_s}{\partial X^2} + \frac{\partial^2\theta_s}{\partial Y^2}\right] + Nu_{fs}\left(\theta_{nf} - \theta_s\right) = 0, \tag{10}$$

The thermal physical characteristics that define the effective thermophysical properties of a working nanofluid as a function of the nanoparticle concentration are as follows: the dynamic viscosity μ_{nf}, the density ρ_{nf}, the coefficient of thermal expansion $(\rho\beta)_{nf}$, the capacitance of heat $\left(\rho C_p\right)_{nf}$, and the thermal conductivity k_{nf} [55,56]. The following equations can be used to establish these thermal properties:

$$\rho_{nf} = (1-\varphi)\rho_f + \varphi\rho_{np}, \tag{11}$$

$$\mu_{nf} = (1+2.5\varphi)\mu_f, \tag{12}$$

$$(\rho\beta)_{nf} = (1-\varphi)(\rho\beta)_f + \varphi(\rho\beta)_{np}, \tag{13}$$

$$\left(\rho C_p\right)_{nf} = (1-\varphi)\left(\rho C_p\right)_f + \varphi\left(\rho C_p\right)_{np}, \tag{14}$$

$$\frac{k_{nf}}{k_f} = \left[\frac{k_{np} + 2k_f - 2\varphi\left(k_f - k_{np}\right)}{k_{np} + 2k_f + \varphi\left(k_f - k_{np}\right)}\right], \tag{15}$$

The thermophysical properties of the water-based fluid and the copper nanoparticles are listed in Table 1.

Table 1. Thermophysical properties of water and copper [55,56].

Property	$\rho(kg/m^3)$	Cp(J/kg.K)	k(W/m.K)	$\beta(1/K)$	$\mu(kg/m.s)$
Water	996.4	4178.56	0.61	2.1×10^{-4}	855×10^{-6}
Copper	8933	385	400	1.67×10^{-5}	-

The boundary conditions of the current problem in a non-dimensional arrangement can be formulated as follows:

$U = 0, V = 0, \theta_f = \theta_s = 1$ on the left isothermal wall;

$U = 0, V = 0, \frac{\partial \theta_f}{\partial Y} = \frac{\partial \theta_s}{\partial Y} = 0$ on the bottom wall;

$U = 0, V = 0, \frac{\partial \theta_f}{\partial Y} = \frac{\partial \theta_s}{\partial Y} = 0$ on both top walls;

$U = 0, V = 0, \frac{\partial \theta_f}{\partial X} = \frac{\partial \theta_s}{\partial X} = 0$ on the right adiabatic wall;

$U = 0, V = -1, \theta_f = \theta_s = 0$ on the inlet port;

$$U = 0, \ \frac{\partial \theta_f}{\partial Y} = \frac{\partial \theta_s}{\partial Y} = \frac{\partial V}{\partial Y} = 0 \ \text{ on the outlet port.} \tag{16}$$

To assess the heat transmission rate from the left wall to the metal foam zone within the enclosure, the local value of the Nu number for the nanofluid and solid matrix phases can be respectively expressed as follows:

$$Nu_{nf} = -\frac{k_{nf}}{k_f}\left(\frac{\partial \theta_{nf}}{\partial n}\right)_n, \tag{17}$$

$$Nu_s = -\frac{k_s}{k_f}\left(\frac{\partial \theta_s}{\partial n}\right)_n, \tag{18}$$

The mean value of the Nu number can be determined by integrating the local mean value along the left sidewall, and can be respectively stated as follows:

$$\overline{Nu}_{nf} = \frac{1}{S}\int_0^S Nu_{nf} ds, \tag{19}$$

$$\overline{Nu}_s = \frac{1}{S}\int_0^S Nu_s ds, \tag{20}$$

where n and S stand for the gradient along the normal direction and the length of the left vertical sidewall, respectively. Equations (17)–(20) were employed for the straight and corrugated left vertical sidewalls.

3. Grid Independence and Code Validation

Governing Equations (6)–(15), subjected to the boundary conditions stated in Equation (16), were solved numerically by employing the finite volume method to establish isotherm lines, the streamline field, and the Nu number throughout the cavity. A numerical simulation was performed by employing the ANSYS FLUENT version 2023 commercial software. The geometry of the two-dimensional L-shaped vented enclosure under examination in the present study was tested using grid size susceptibility tests to calculate the adequacy of the meshing scheme and to confirm that the results were grid-independent, as shown in Tables 2 and 3. The grid refinement test was performed for the non-corrugated and corrugated cases with specific parameter values. For the non-corrugated cavity case, the parameters were set to be $Re = 20$, $\frac{D}{H} = 0.3$, and $\varphi = 5\%$ (Table 2), while the parameters

for the corrugated enclosure case were $Re = 500$, $\frac{D}{H} = 0.2$, $N = 5$, $CR = 1$, and $\varphi = 5\%$ (Table 3). The results demonstrate that the average Nu of the nanofluid and solid phases changed very little (less than 1%), with an element number of 1,588,132 compared to an element number of $1,333,000$ for the non-corrugated enclosure. Moreover, the average Nu of the two phases exhibited a very small change (less than 1%), with an element number of 1,799,990 compared to an element number of 1,487,182 for the corrugated cavity. Therefore, the element numbers of 1,333,000 and 1,487,182 were adopted for both the non-corrugated and corrugated cases in the present study, since these element numbers met the mutual requirements of the study in terms of grid independency and the computation time limits.

Table 2. Grid-independent assessment: fluid-phase and solid-phase average Nu number near the left sidewall of the non-corrugated cavity, utilizing numerous mesh sizes.

No. of Elements	13,300	47,188	120,000	188,000	245,960	480,000	750,000	1,333,000	1,588,132
$\overline{Nu}_{nf}$	0.98898	0.99706	0.99939	1.00071	1.00429	1.00258	1.00452	1.0046	1.00483
$\overline{Nu}_{s}$	18.4963	19.5636	20.0519	20.2031	20.3419	20.3849	20.4717	20.485	20.4999

Table 3. Grid-independent assessment: fluid-phase and solid-phase average Nu number near the left sidewall of the corrugated cavity, utilizing numerous mesh sizes.

No. of Elements	28,640	44,110	138,356	230,750	452,750	703,010	970,536	1,487,182	1,799,990
$\overline{Nu}_{nf}$	7.942	7.979	7.903	7.885	7.802	7.812	7.843	7.788	7.743
$\overline{Nu}_{s}$	163.873	164.729	163.084	162.619	160.908	161.083	161.659	160.587	159.659

To validate the numerical results of the present model, two validations were performed against similar investigations in the literature. The first validation, shown in Figure 2, utilized the numerical streamline and isotherm results of ref. [43] for the mixed-convection heat transfer of a nanofluid in a ventilated cavity at $Re = 500$, $Ri = 1$ (Richardson number, $Ri = Gr/Re^2$), and $\varphi = 5\%$. Furthermore, the second validation was accomplished with the results obtained in ref. [8] for natural convection inside an enclosure occupied by a nanofluid-saturated porous medium with a local thermal non-equilibrium. This validation was performed for the case of $Ra = 10$, $\varepsilon = 0.5$, and $\varphi = 2\%$, and the contours of the streamline and the fluid- and solid-phase temperatures of the porous medium is described in Figure 3. From both verifications above, it was evident that the current simulation supported the numerical results in the literature with an elevated degree of precision. In addition, these verifications demonstrated the excellent correspondence between the behavior results and the values of the flow and heat field contours.

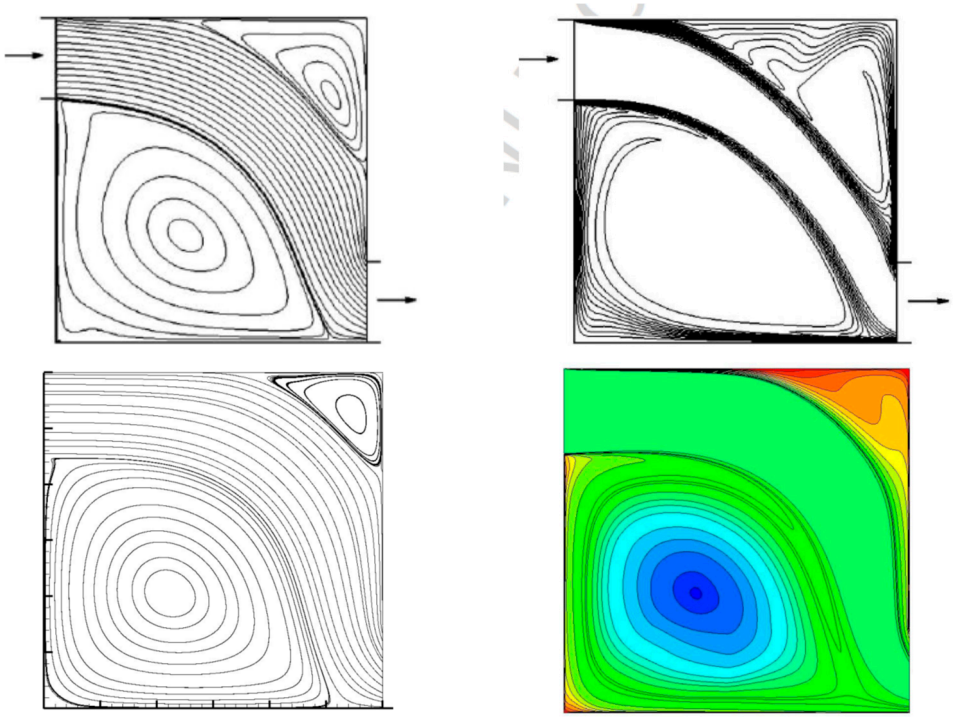


Figure 2. Streamline field (**left**) and isotherm lines (**right**), comparing ref. [43] and the present work (**lower row**) at $Re = 500$, $Ri = 1$, and $\varphi = 5\%$.

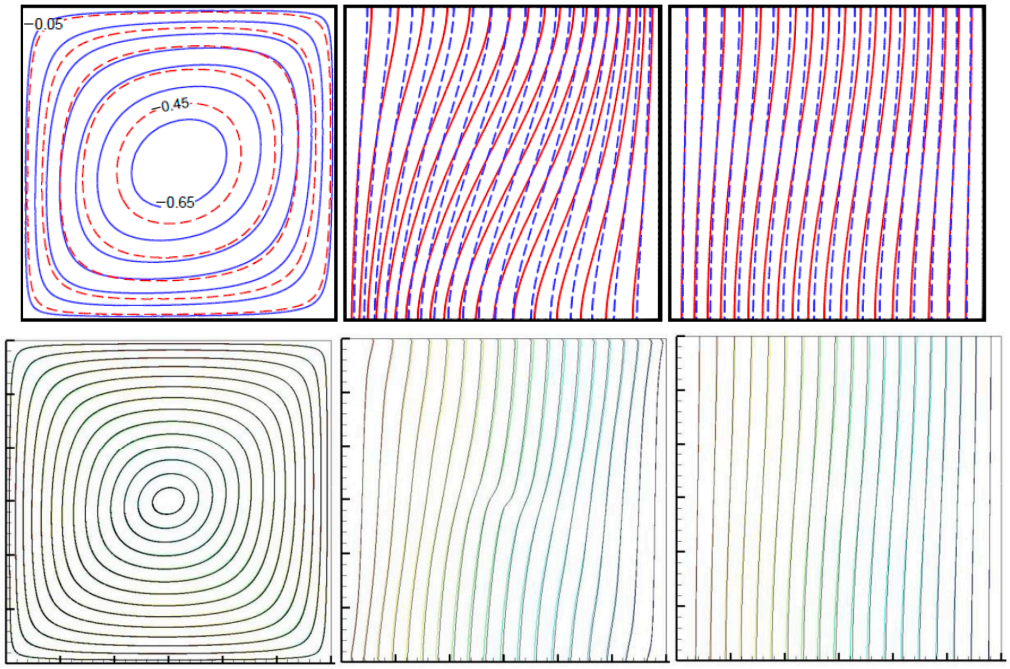


Figure 3. Streamline field (**left**), isotherm lines of fluid phase (**middle**), and isotherms of solid phase (**right**), comparing ref. [8] and the present work (**lower row**) for pure water (solid lines) and the hybrid nanofluid (dash lines) at $Ra = 10$, $\varepsilon = 0.5$, and $\varphi = 2\%$.

4. Results and Discussions

To examine the heat transfer performance for L-shaped vented cavities occupied with copper metal foam, the temperature and streamline profiles inside the cavity of the isothermal left vertical sidewall and the other insulated walls were obtained numerically. The metal foam, with a pores per inch ($PPI = 10$), was saturated with a copper nanofluid

with different nanoparticle concentrations. The cavity had equal dimensions for its length and height ($H = L$). Two types of geometry for the left-side vertical wall were considered: a non-corrugated (straight) sidewall and a corrugated wall with various corrugation numbers and dimensions. These two cases were analyzed broadly for the widespread range of the pertinent parameters, as described in the two sections below.

4.1. Non-Corrugated Vertical Left Sidewall

When the left sidewall was straight (non-corrugated), the main goals were to investigate the effects of the Reynolds number, the aspect ratios of the inflow and outflow vents' width-to-height length, and the nanofluid solid fraction on the flow field and isotherms. These relevant parameters ranged from 20 to 1000 for the Reynolds number, and the range of the aspect ratio was $D/H = 0.1$–0.4, while the nanoparticle volume proportions varied from $\varphi = 0\%$ (pure water) to 20%.

The streamlines and fluid and solid isotherm fields for Reynolds number values of 20, 500, and 1000; the inflow and outflow aspect ratios of 0.1 and 0.4; and the nanoparticle volume fractions of 0% and 20% are illustrated in Figures 4, 5, and 6, respectively. It is apparent from these three figures that raising the Reynolds number leads to an intensification of the streamlines and higher values at the enclosure inlet and sharp edge, especially when the inflow-to-outflow vent aspect ratio is augmented to 0.4. This is because of the high velocity values and the increasing width value at the inlet, which results in a more free flow of fluid with higher inertial force values, and there was no constraint or impedance on the fluid flow compared with a value of 0.1 for the inlet-to-outlet aspect ratio. The addition of copper nanoparticles to the base fluid (water) caused the fluid to become more viscous; thus, the velocity of the fluid decreased slightly and the streamlines became conspicuously more intense at the enclosure edge area compared with the case when the cavity was filled with a pure fluid, with $\varphi = 0\%$. This behavior led to a reduction in the fluid-phase compared to the solid-phase temperature, as shown in Figures 5 and 6, in addition to other reasons that stand behind this difference in temperature between the fluid and solid phases of the metal foam, such as the difference in their heat capacity and thermal conductivity. The presence of copper nanoparticles in the fluid led to an increase in the fluid-phase temperature due to an increase in the nanofluid thermal conductivity, which resulted in a higher heat transfer rate among the two phases of saturated metal foam. Increasing the Reynolds number and the aspect ratios of the inflow and outflow vents tended to increase the temperature of the solid and fluid metal foam phases because of the same reasons mentioned for the streamline behavior. Furthermore, as the Reynolds number and vent aspect ratios increased, forced convection currents generated from amplifying the inertia forces and the boundary layer thickness increased, which resulted in a higher heat transfer rate and, thus, higher solid and fluid temperature values. Higher temperature values exhibit amplifying values of the Nusselt number that are proportional to the Reynolds number, the aspect ratios of the openings, and the nanofluid concentration fraction.

From the temperature contours, it was also observable that the thermal boundary layer was distinct in the enclosure, especially near the hot wall, which means that the heat transfer rate due to convection is of considerable value. This is clearly clarified by the Nu values of both the fluid and solid metal foam phases, as established in Figures 7 and 8. By inspecting these two figures, it can be deducted that the fluid phase of the copper metal foam's Nu number near the hot left sidewall increased with an increase in the nanoparticle concentration volume ratio, while the solid-phase Nusselt number decreased. The fluid-phase Nusselt number rose by 26% at $Re = 1000$ and $D/H = 0.3$, and by 52.9% at $Re = 20$ and $D/H = 0.4$, whereas the solid-phase Nusselt number decreased by 11% at $Re = 20$ and $D/H = 0.4$, and by 28% at $Re = 1000$ and $D/H = 0.1$ when the nanoparticle volume

fraction was varied from 0% to 20%. The increase in the fluid-phase Nusselt number was attributed to the increase in the nanofluid thermal conductivity and the reduced heat capacity, resulting in a higher heat transfer rate and a temperature gradient near the wall. This led to an increase in the convection currents in this phase, and thus, the Nusselt number increased. On the other hand, the Nusselt number of the solid phase decreased with an increase in the nanoparticle intensity; this was due to a reduction in the solid-phase temperature gradient. This occurred because the nanofluid thermal conductivity increased, which resulted in a higher degree of heat transmission between the fluid and solid phases, thus inducing a lower solid-phase temperature gradient. In general, it was observed that the Nusselt number for the two phases of metal foam intensified largely with the amplification of the *Re* number compared with the minor alteration when the ratio of the inflow and outflow vent dimension to the height dimension was raised. At $\varphi = 20\%$, the fluid-phase Nusselt number rose by 367.56% at $D/H = 0.2$ and by 315.38% at $D/H = 0.4$, whereas the solid-phase Nusselt number increased by 388.28% at $D/H = 0.2$ and by 347.52% at $D/H = 0.4$ when the *Re* number was augmented from 20 to 1000. Generally, the fluid and solid Nusselt numbers rose by around 3.5 times when the Reynolds number increased from 20 to 1000. Increasing the Nusselt number of both phases was attributed to forced convection currents growing as the fluid velocity rises when the inertia forces (Reynolds number) intensify. It could also be perceived that amplifying the inlet and outlet opening port dimensions reduced the percentage increase, due to the amplification of the cold fluid volume flowing into the enclosure. This increasing cold fluid volume absorbed more heat from the left hot wall, which resulted in a temperature gradient reduction for the nearby wall compared to the smaller opening vent dimensions.

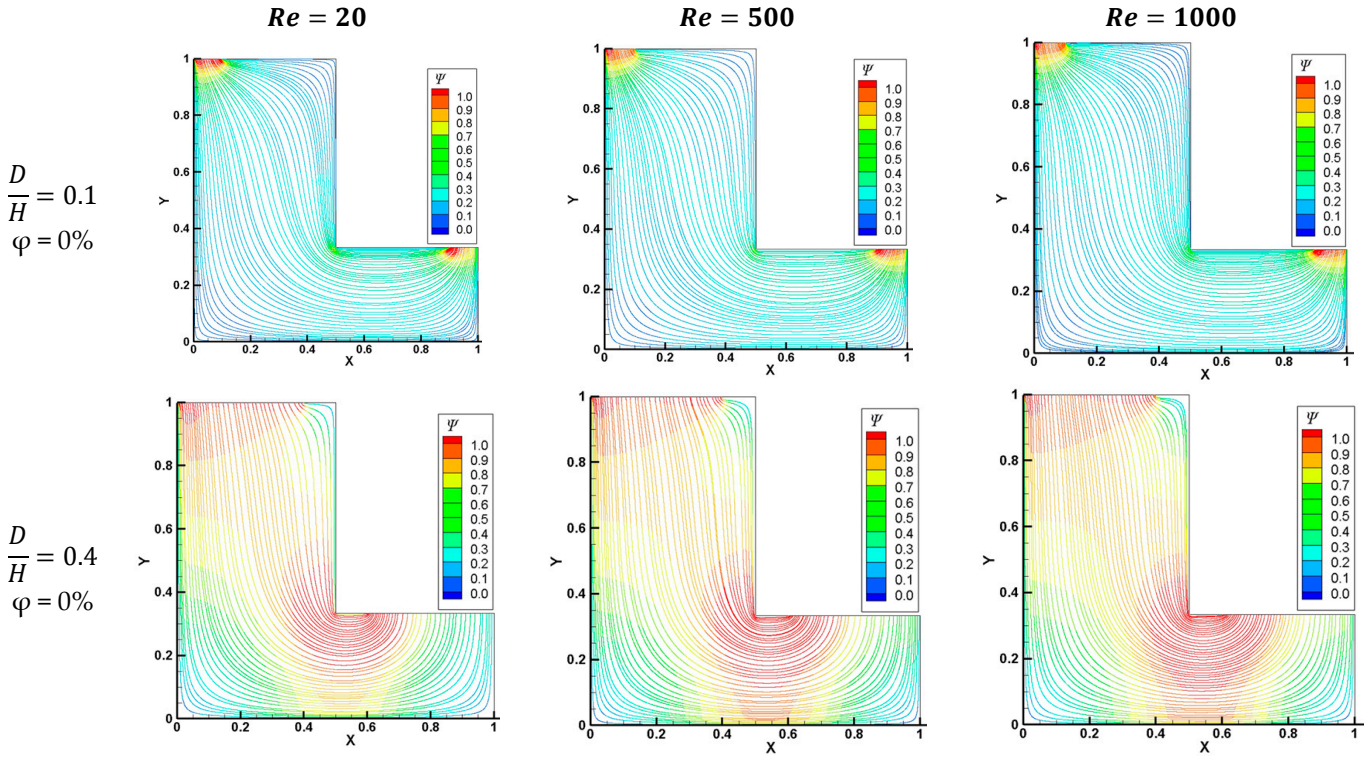


Figure 4. *Cont.*

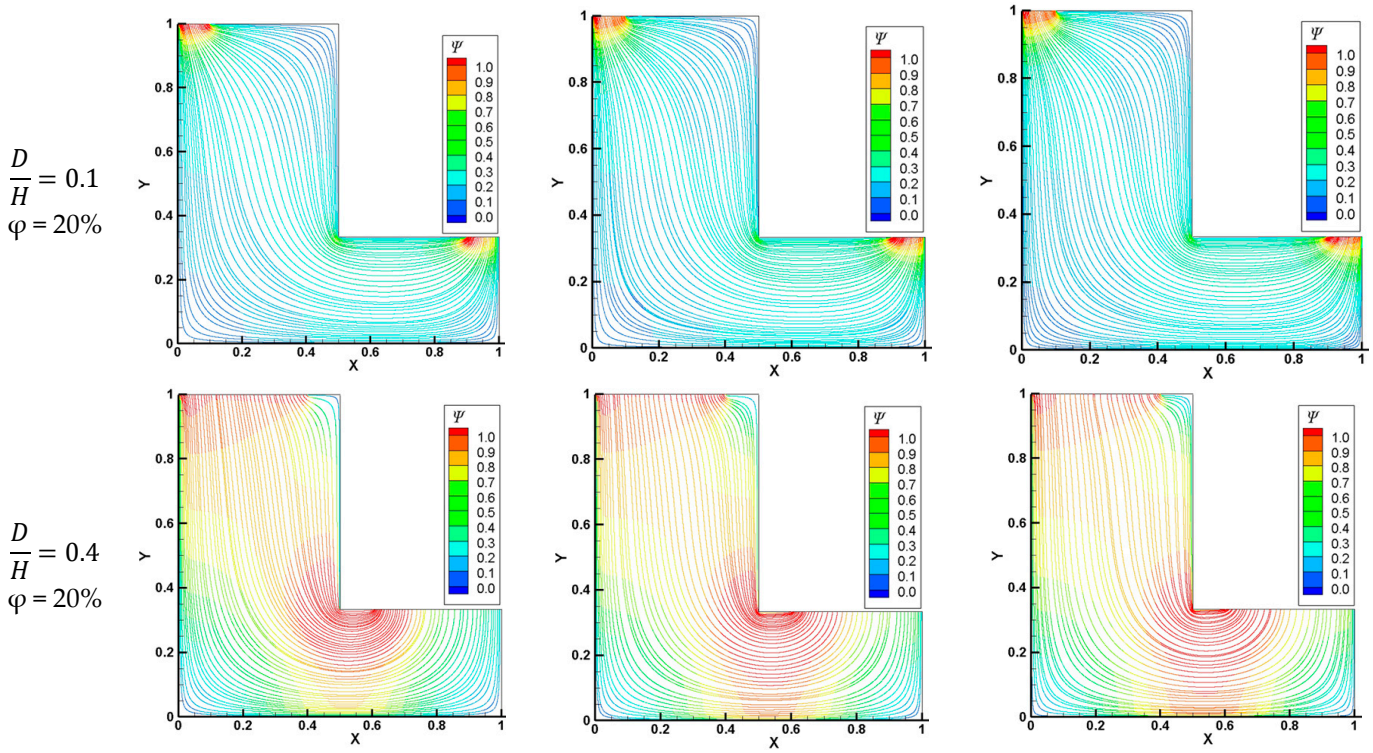


Figure 4. Streamlines for various values of Reynolds number, inflow and outflow aspect proportions, and nanoparticle volume fractions.

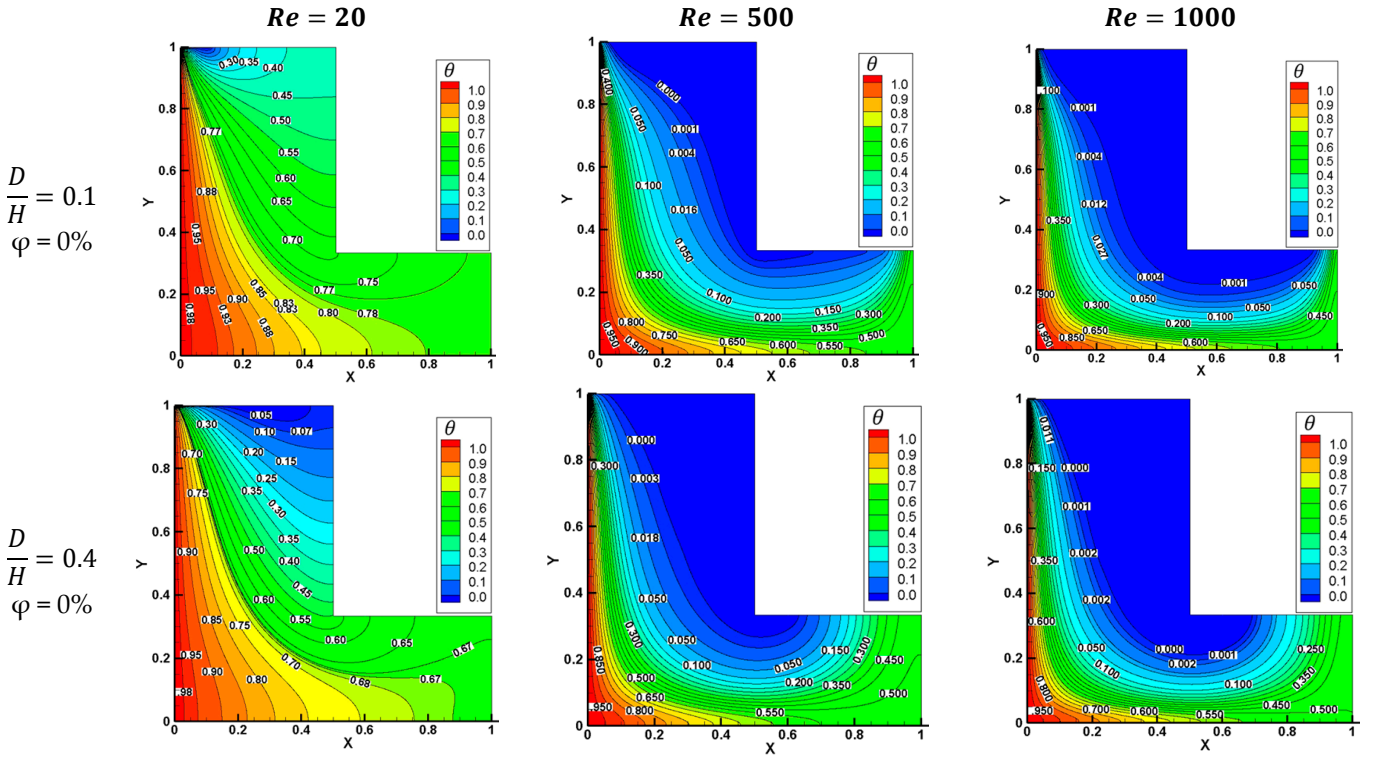


Figure 5. *Cont.*

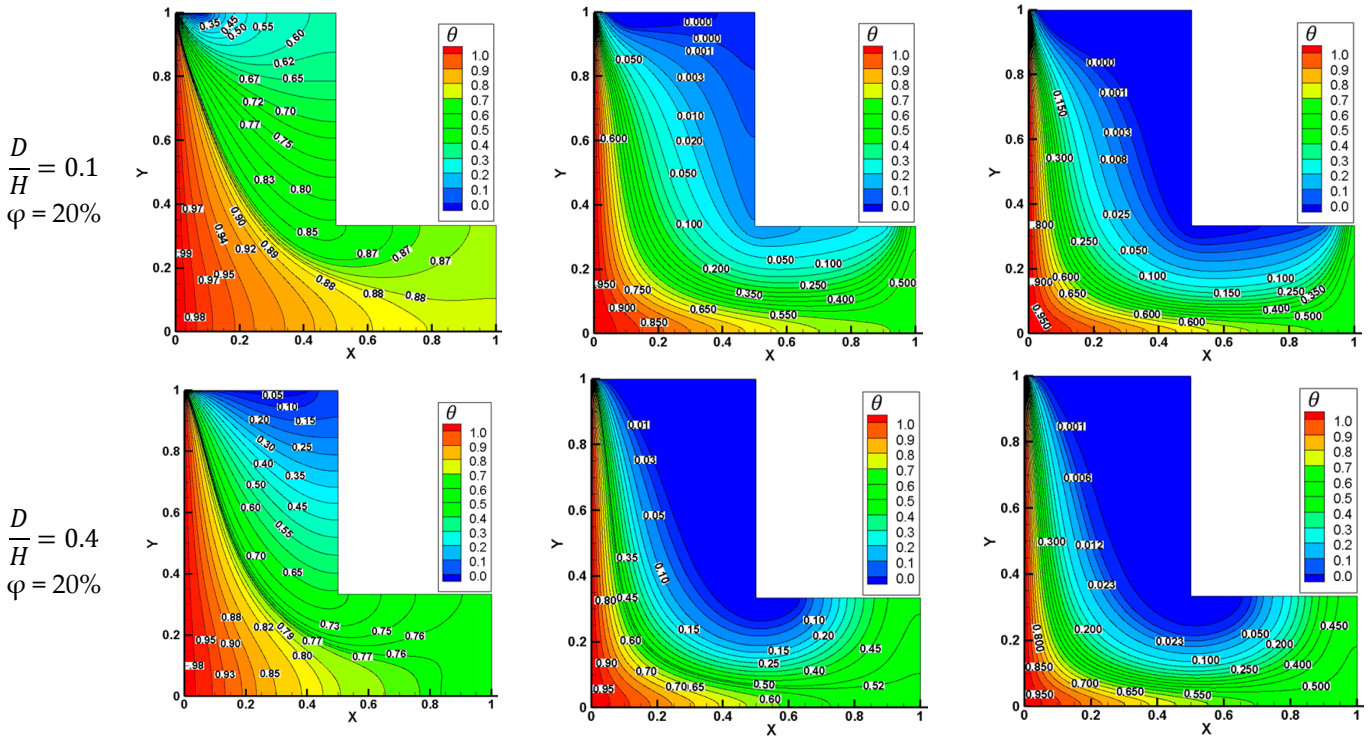


Figure 5. Fluid-phase isotherms for various values of Reynolds number, inflow and outflow aspect proportions, and nanoparticle volume fractions.

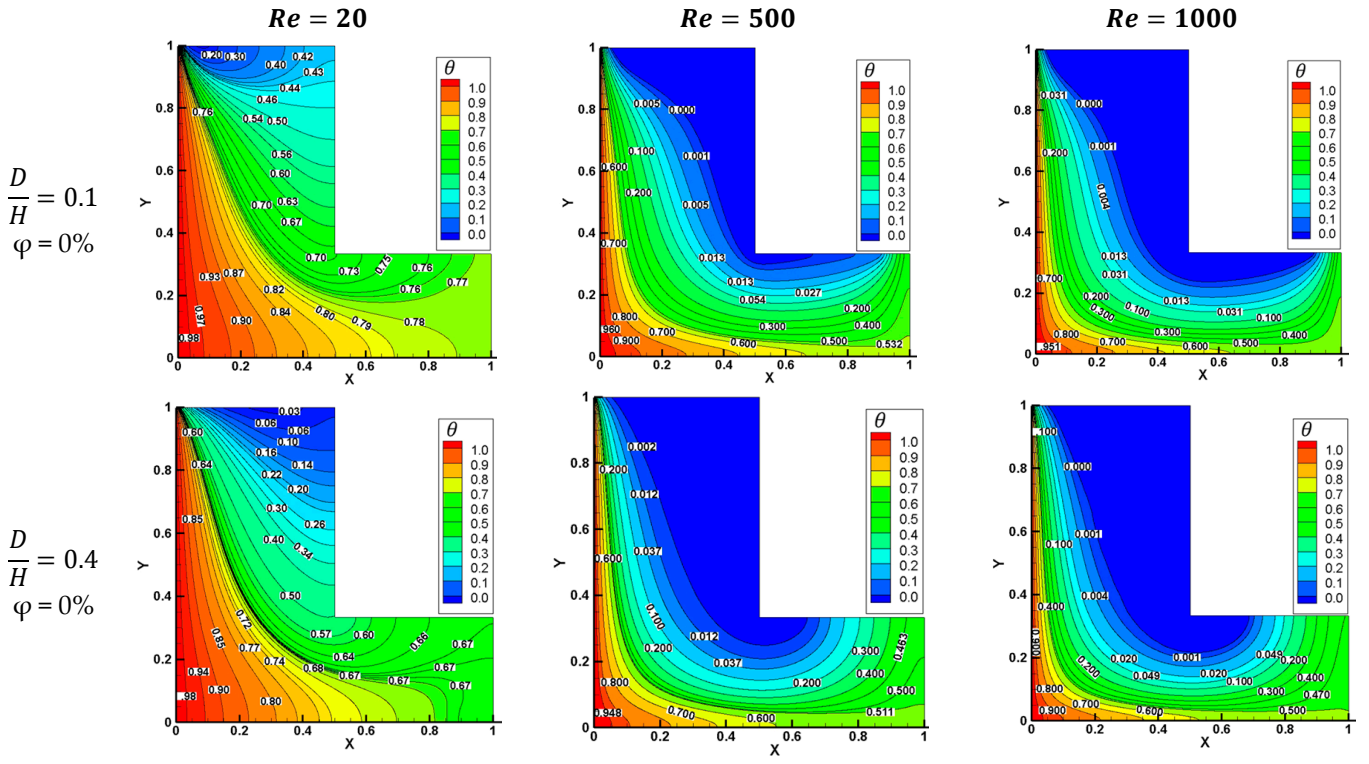


Figure 6. *Cont.*

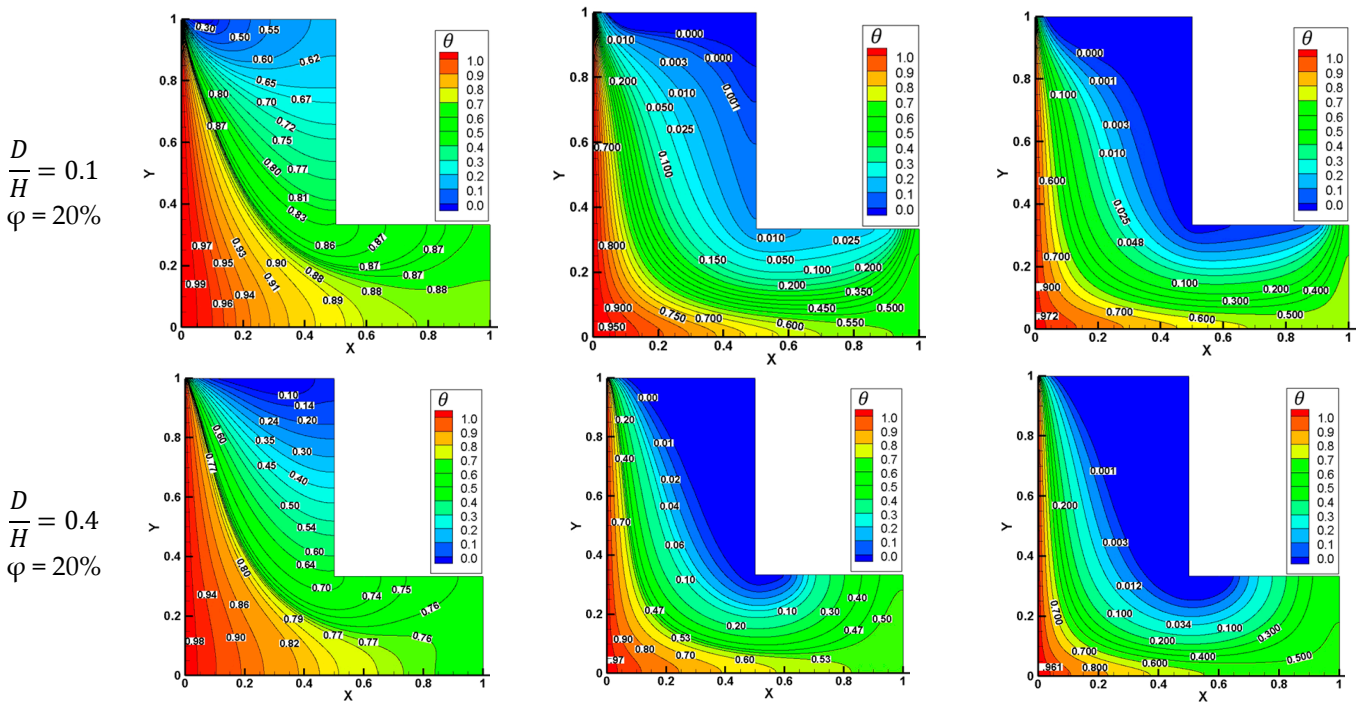


Figure 6. Solid-phase isotherms for various values of Reynolds number, inflow and outflow aspect proportions, and nanoparticle volume fractions.

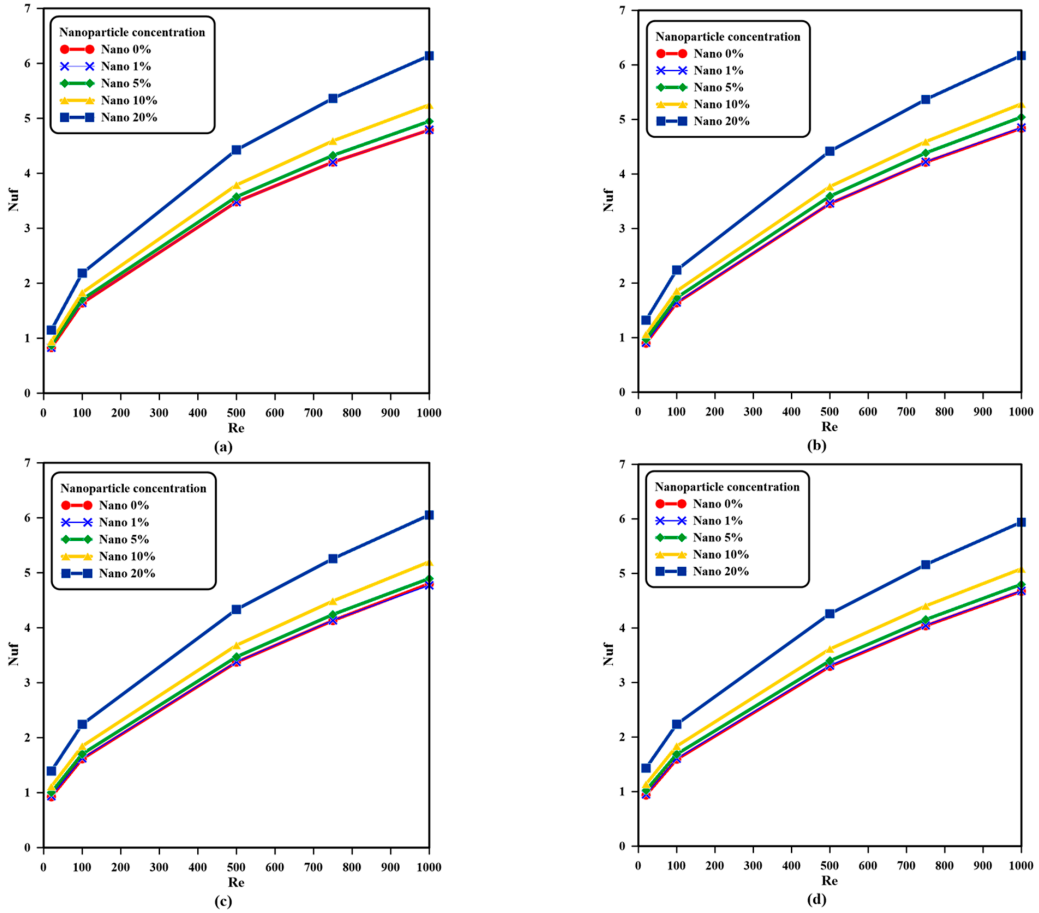


Figure 7. Nusselt number of fluid-phase alterations vs. Reynolds number, with different values of inflow and outflow aspect proportion and nanofluid concentration fraction: (**a**) $D/H = 0.1$; (**b**) $D/H = 0.2$; (**c**) $D/H = 0.3$; and (**d**) $D/H = 0.4$.

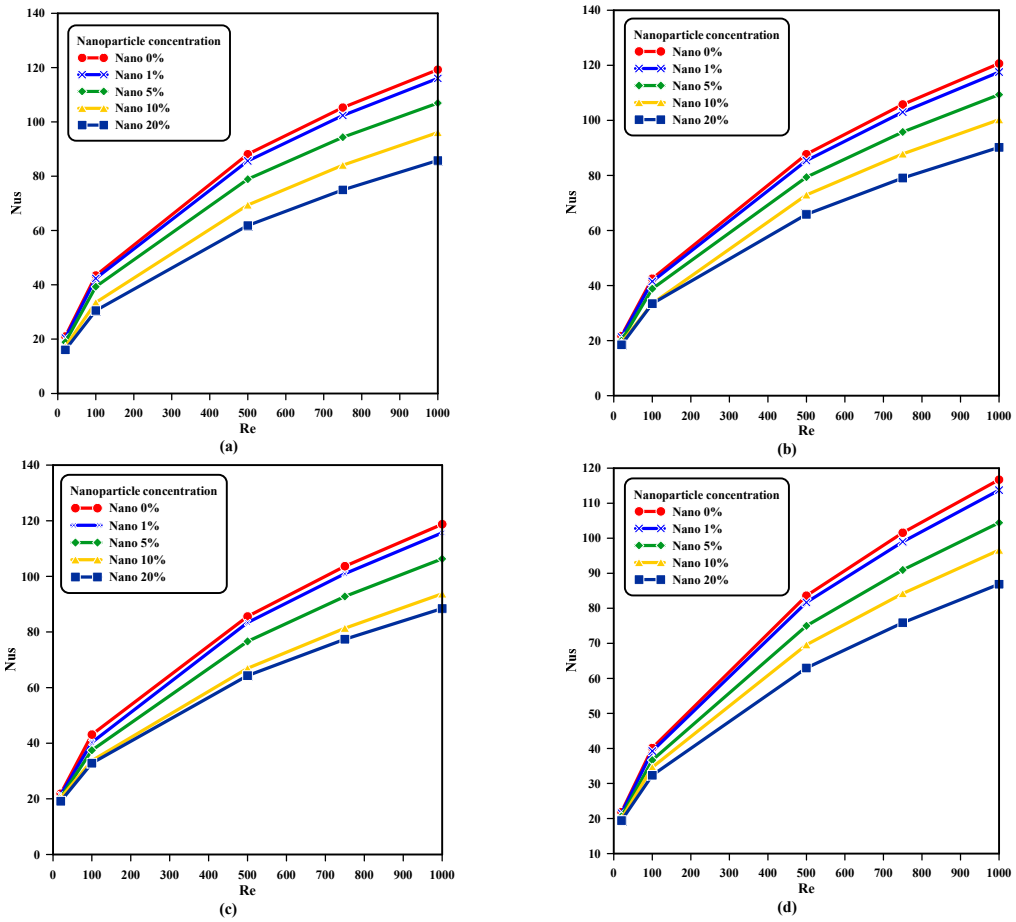


Figure 8. Nusselt number of solid-phase alterations vs. Reynolds number, with different values of inflow and outflow aspect proportion and nanofluid concentration fraction: (**a**) $D/H = 0.1$; (**b**) $D/H = 0.2$; (**c**) $D/H = 0.3$; and (**d**) $D/H = 0.4$.

4.2. Corrugated Vertical Left Sidewall

The case with a corrugated left sidewall was also performed in the present investigation. Corrugation with a rectangular-geometry-type wave form and dimensions of a and b (shown in Figure 1b) was taken into consideration, and the ratio of the dimensions, expressed as the corrugation ratio ($CR = a/b$), was studied for two values: $CR = 1$ and $CR = 0.5$. Additionally, the number of rectangular corrugations N was included and interpreted as $N = 5$ or $N = 10$. The thermal performance of the Re number varying from 20 to 1000 and an aspect ratio of the inflow and outflow vents of 0.1 or 0.4 was implemented.

The contours of the streamlines and the fluid- and solid-phase isotherms for different values of the corrugation ratio CR and the frequency N are illustrated in Figures 9–11. As the corrugation ratio was increased from 0.5 to 1, the penetration of the fluid towards the cavity's left sidewall pockets became more difficult, and small re-circulation zones were established within those pockets. On the other hand, the isotherm distribution of the fluid and solid phases of the metal foam showed less clustering behavior near the cavity pockets, indicating an inefficient heat transfer process in those regions with increasing height. Moreover, vortices were established in the rectangular pockets, and as the number of rectangular corrugated pockets increased, less flow penetrated the pockets and very weak flow circulation was observed in those regions. In addition, the fluid and solid temperature gradients were reduced in the rectangular pockets of the hot sidewall surface as the number of pockets increased from $N = 5$ to $N = 10$. For all the above studied cases, variation in the effect of the Re number is also depicted in the corresponding figures, and its effect is clearly indicated on the streamlines and the thermal boundary layer thickness

and shape. Moreover, an increase in the *Re* number tended to result in an increase in the heat transfer rate inside the cavity because of forced convection currents intensifying by means of a higher velocity of fluid inside the cavity. A high cold fluid velocity and inertia transmitted excessive energy from the heated wall, and a superfluous temperature gradient was achieved. Accordingly, elevated fluid- and solid-phase Nusselt numbers were obtained, and their quantitative responses among the studied relevant parameters are discussed below.

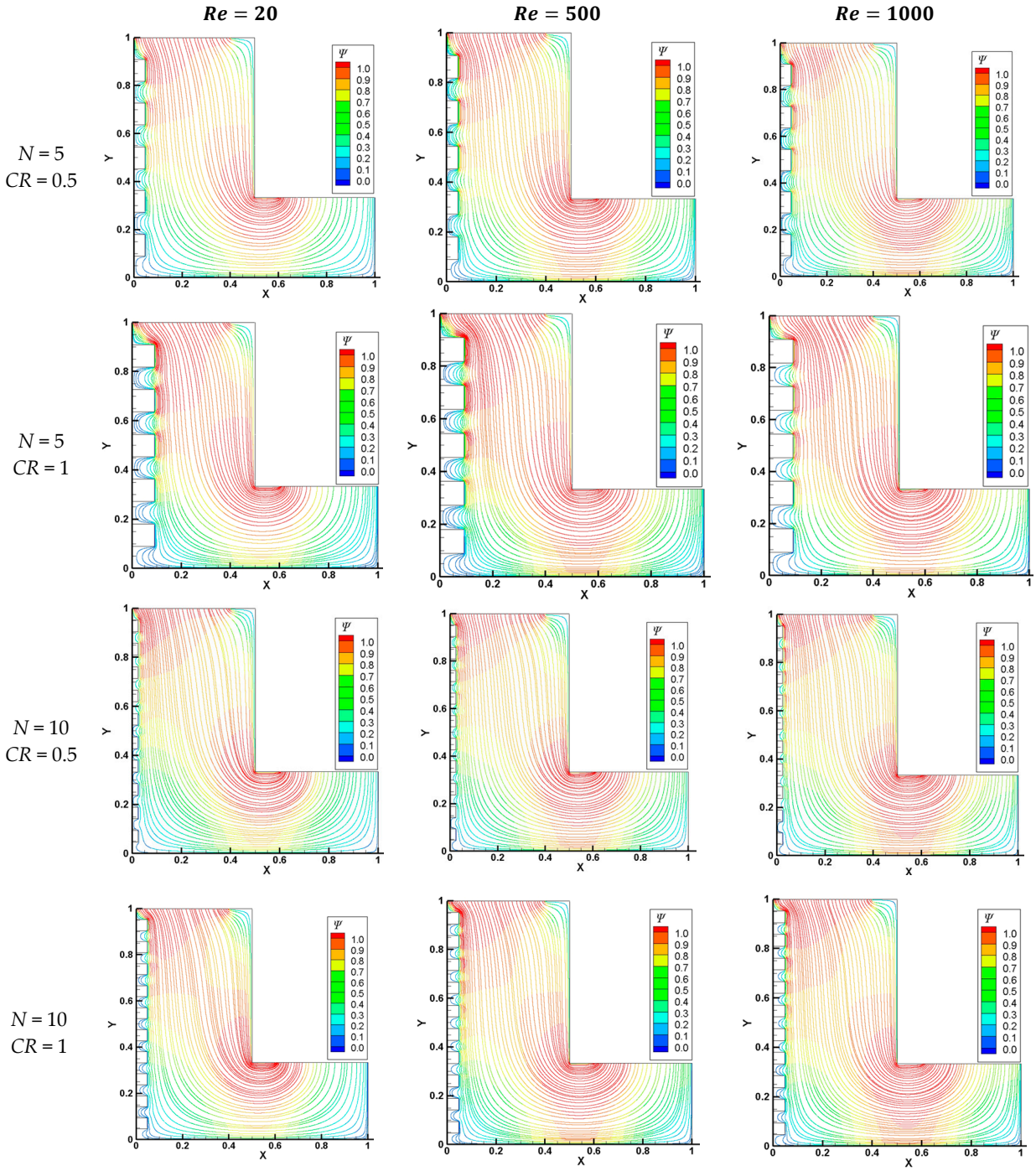


Figure 9. Streamlines for various values of Reynolds number, inflow and outflow aspect proportions, and nanoparticle volumes.

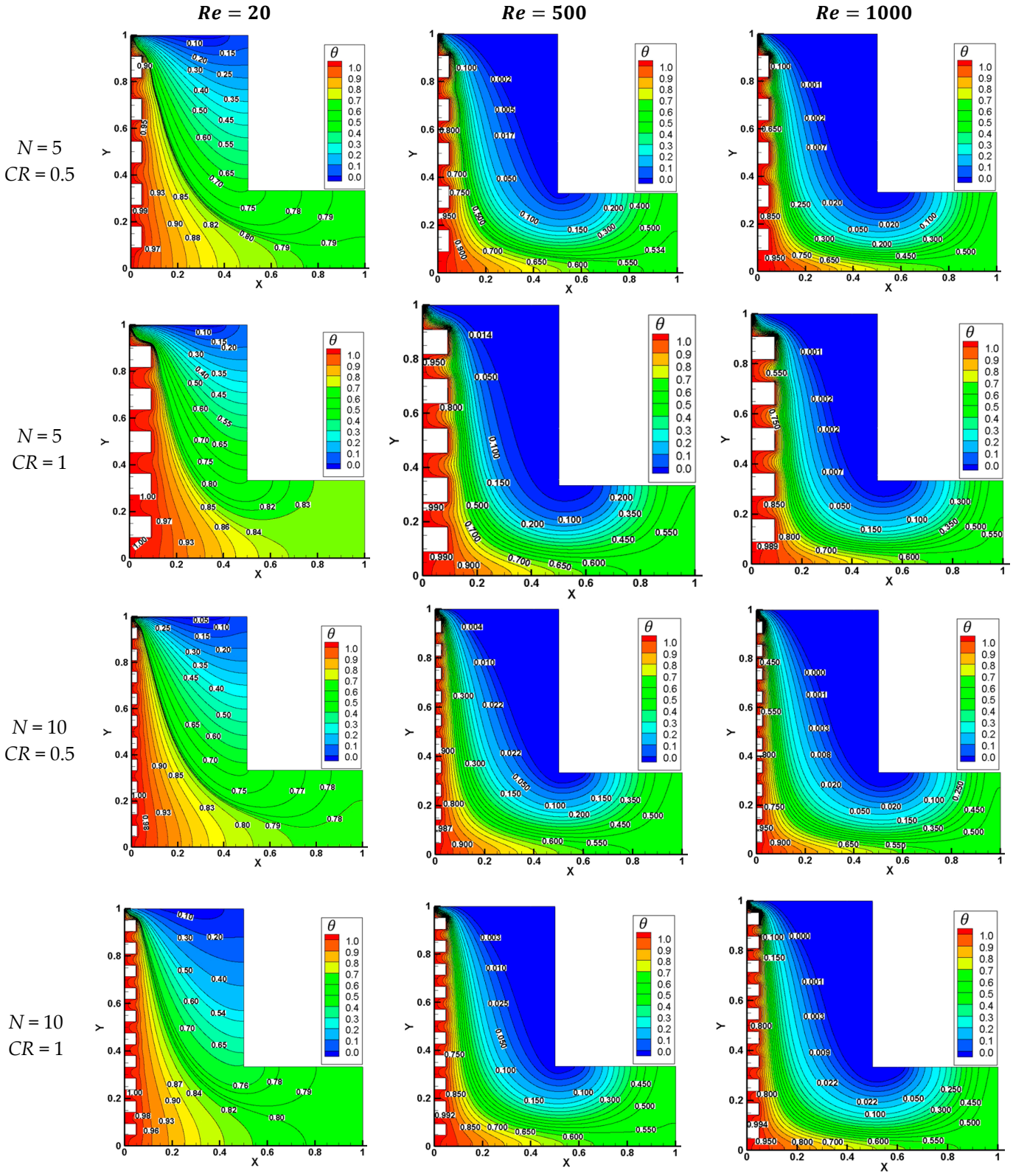


Figure 10. Fluid-phase isotherms for various values of Reynolds number, inflow and outflow aspect proportions, and nanoparticle volumes.

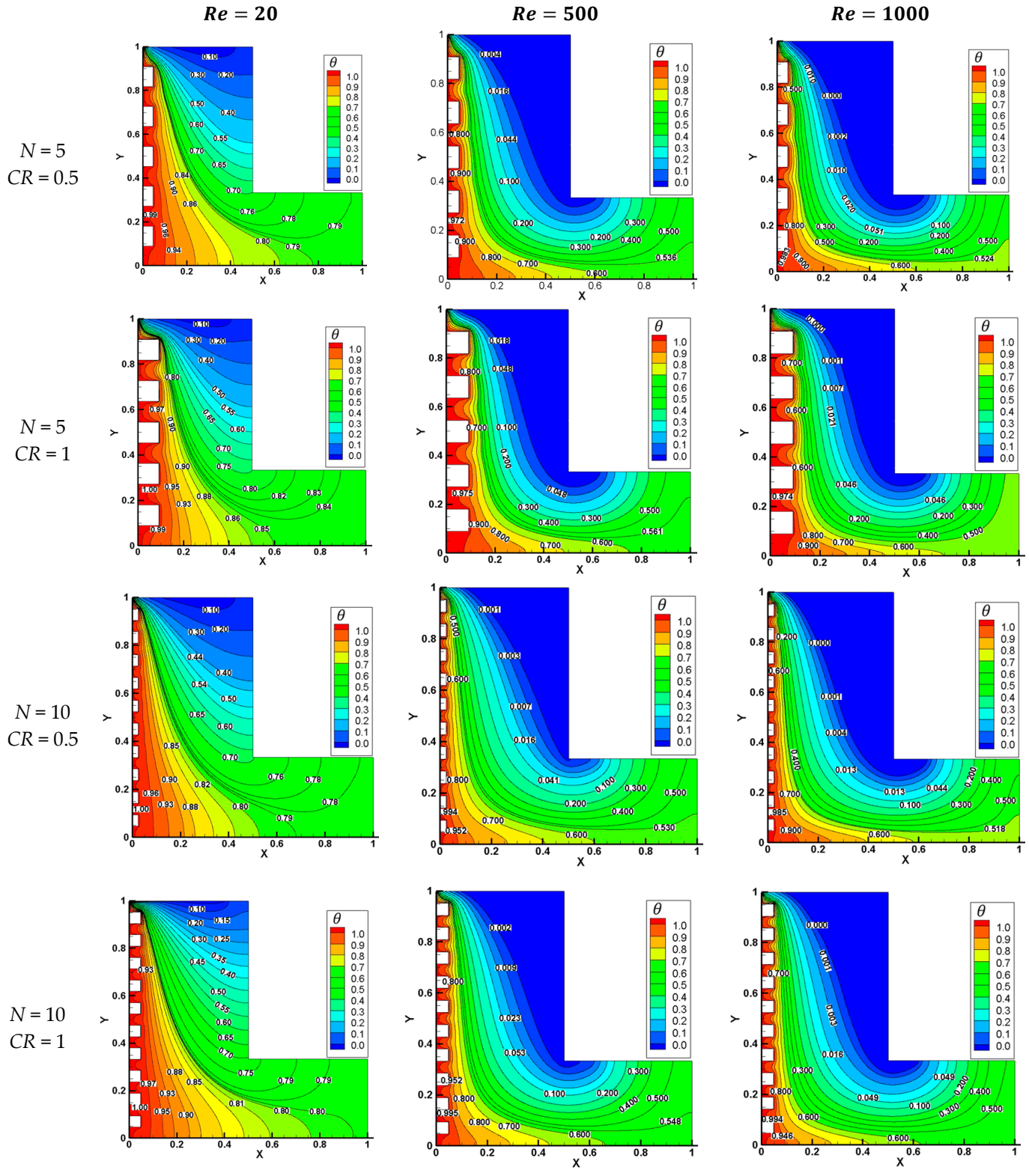


Figure 11. Solid-phase isotherms for various values of Reynolds number, inflow and outflow aspect proportions, and nanoparticle volumes.

The variation in the fluid- and solid-phase Nu number with the Re number is graphed in Figure 12 for different volume fractions of copper nanofluid particles and the values of 0.1 and 0.4 for the inflow and outflow vent aspect fraction. From this figure, at $D/H = 0.4$, $\varphi = 10\%$, $N = 5$, and $CR = 0.5$, it can be determined that the fluid- and solid-phase Nusselt numbers increased by 331.2% and 366.32%, respectively, as the Reynolds number varied in

the range of (20–1000). Commonly, it was deducted that the Nusselt number of the two phases increased by around (3–4) times with an increasing Re number from 20 to 1000. This is owing to an increase in the forced convection currents among the saturated fluid and solid portions of metal foam inside the cavity, which provide a greater temperature gradient near the wall. From this figure, it was also determined that the Nu numbers of the two phases decreased with an increase in the aspect ratio because more cold fluid entered the cavity and transferred heat from the left hot sidewall, which caused a decrease in the temperature gradient beside the wall. When $Re = 750$, $\varphi = 20\%$, $N = 5$, and $CR = 0.5$, it was determined that the fluid- and solid-phase Nusselt numbers decreased by 10.35% and 8.55%, respectively, as the opening aspect ratio was increased from 0.1 to 0.4. In general, the reduction in the fluid and solid Nusselt numbers was approximately 10% when the vent opening aspect ratio was augmented from 0.1 to 0.4. Furthermore, it was found that the fluid-phase Nu number increased and the solid-phase Nu number decreased with an increase in φ for the same reason mentioned in the situation of the non-corrugated wall. The fluid-phase Nusselt number rose by 30% at $Re = 1000$ and $D/H = 0.1$, and by 42% at $Re = 20$ and $D/H = 0.4$, whereas the solid-phase Nusselt number decreased by 9% at $Re = 20$ and $D/H = 0.4$, and by 13% at $Re = 1000$ and $D/H = 0.1$ when the nanoparticle volume fraction was increased from 0% to 20%.

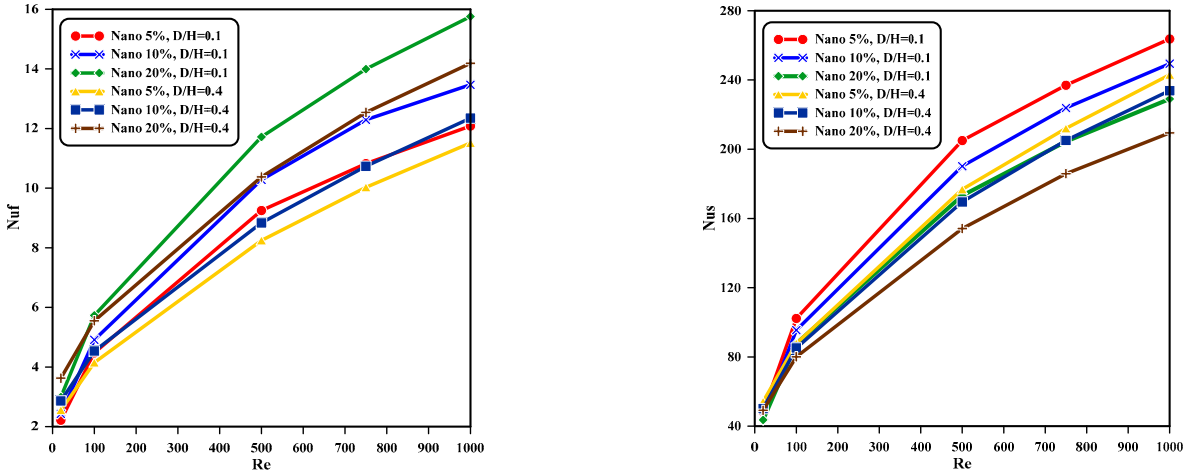


Figure 12. Nusselt number of fluid- and solid-phase alterations with Reynolds number for different values of inflow and outflow proportions and nanoparticle volumes at $N = 5$ and $CR = 0.5$.

From the results obtained for a corrugation wave number of $N = 5$, it is evident that the best concentration of copper nanoparticles in the water base fluid was 20%. Therefore, Figure 13 was utilized to investigate the effect of varying the Re number, the rectangular corrugation wave number, the corrugation ratio, and the inlet and outlet vent ratio for $\varphi = 20\%$. It was observed that the Nu number of the two metal foam phases increased with an increase in the Re number, while it decreased with an increase in the other relevant parameters mentioned above. Quantitively, the Nusselt number increased by around (2–4) times when the Reynolds number rose from 20 to 1000. For instance, at $D/H = 0.1$, $N = 10$, and $CR = 0.5$, the fluid-phase Nusselt number rose by 417.28%, whereas the solid-phase Nusselt number increased by 298.46% at $D/H = 0.4$, $N = 5$, and $CR = 1$ as the Reynolds number was increased from 20 to 1000. On the other hand, augmenting the corrugation ratio from $CR = 0.5$ to $CR = 1$ at $Re = 500$, $N = 5$, and $D/H = 0.4$ caused the fluid- and solid-phase Nusselt number values to decrease by 13.27% and 19.17%, respectively. In general, as the number of rectangular corrugation waves increased from $N = 5$ to $N = 10$ at $Re = 750$, $CR = 1$, and $D/H = 0.1$, the fluid and solid Nusselt number

values decreased by 32.53% and 36.74%, respectively. This may be assigned to conduction heat transfer mode domination among the convection mode adjacent to the left wall and a less compact temperature gradient in the pocket zones of the corrugated wall.

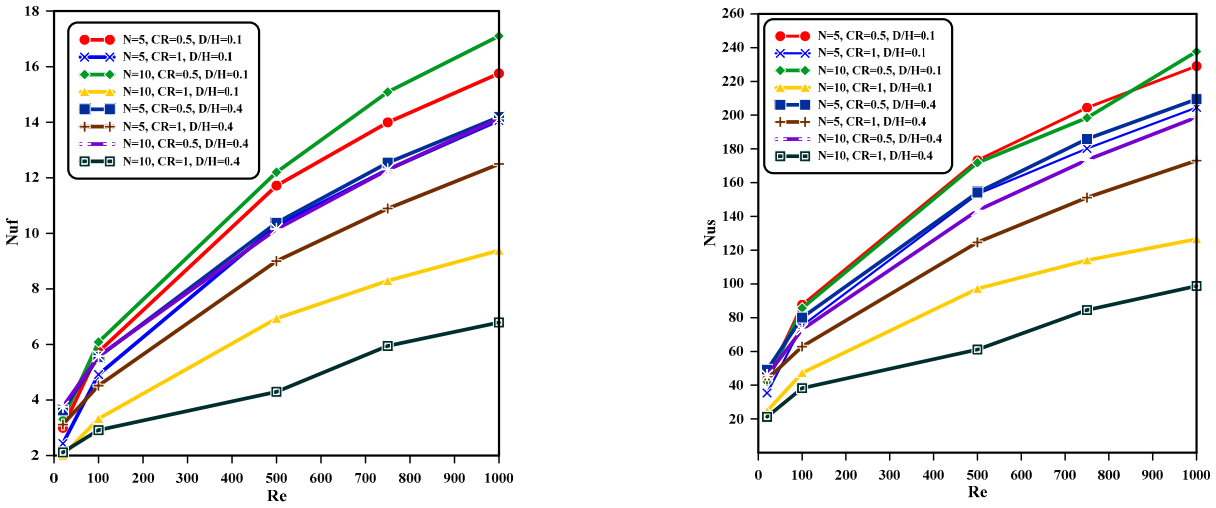


Figure 13. Nusselt number of fluid- and solid-phase alterations vs. Reynolds number for different values of inflow and outflow aspect fractions and numbers of rectangular corrugation waves.

By referring to Figure 13 and based on the predicted results of existing numerical simulations, the related correlated equations of the average fluid- and solid-phase Nusselt numbers based on a Reynolds number range (20–1000) at $N = 5$ for $CR = 0.5,\ 1$ and $D/H = 0.1,\ 0.4$ are expressed as follows in Table 4:

Table 4. Correlations of fluid- and solid-phase Nusselt numbers.

Case	Correlation Expression	Coefficient of Determination R^2
$CR = 0.5$ and $D/H = 0.1$	$\overline{Nu}_{nf} = 0.8201Re^{0.4275}$ $\overline{Nu}_{s} = 12.2926Re^{0.4247}$	0.9996 0.9999
$CR = 1$ and $D/H = 0.1$	$\overline{Nu}_{nf} = 0.6273Re^{0.4496}$ $\overline{Nu}_{s} = 9.3703Re^{0.4478}$	0.9999 0.9996
$CR = 0.5$ and $D/H = 0.4$	$\overline{Nu}_{nf} = 1.1961Re^{0.3521}$ $\overline{Nu}_{s} = 15.3274Re^{0.3744}$	0.9902 0.9945
$CR = 1$ and $D/H = 0.4$	$\overline{Nu}_{nf} = 0.9731Re^{0.3617}$ $\overline{Nu}_{s} = 13.6519Re^{0.3599}$	0.981 0.981

In order to demonstrate the effect of wall corrugation compared to wall non-corrugation, Figures 14 and 15 show the results for different Reynolds number values, rectangular corrugation wave numbers, corrugation ratios, and inflow and outflow vent aspect proportions. From these two figures, it was determined that the fluid-phase and solid-phase Nusselt numbers for the corrugated wall were higher than those for the non-corrugated wall, regardless of the number of corrugations or the corrugation ratio. On the other hand, it is clear that amplifying the corrugation number leads to result in a reduction in the value of Nusselt number for all other relevant parameters. As a result, corrugation is a good option for enhancing thermal performance, but with a smaller number of corrugations; otherwise, the conduction heat transfer mode can be greater than the convection mode and the Nusselt number will decrease. Generally, selecting the number of corrugations depends mainly on the practical engineering application. For example,

$N = 5$ corrugations and a $CR = 1$ can be utilized to corrugate walls and achieve a high Reynolds number in solar air heaters, solar dryers, green building heating, and electronic cooling in order to achieve a remarkable heat transfer enhancement without substantial flow resistance.

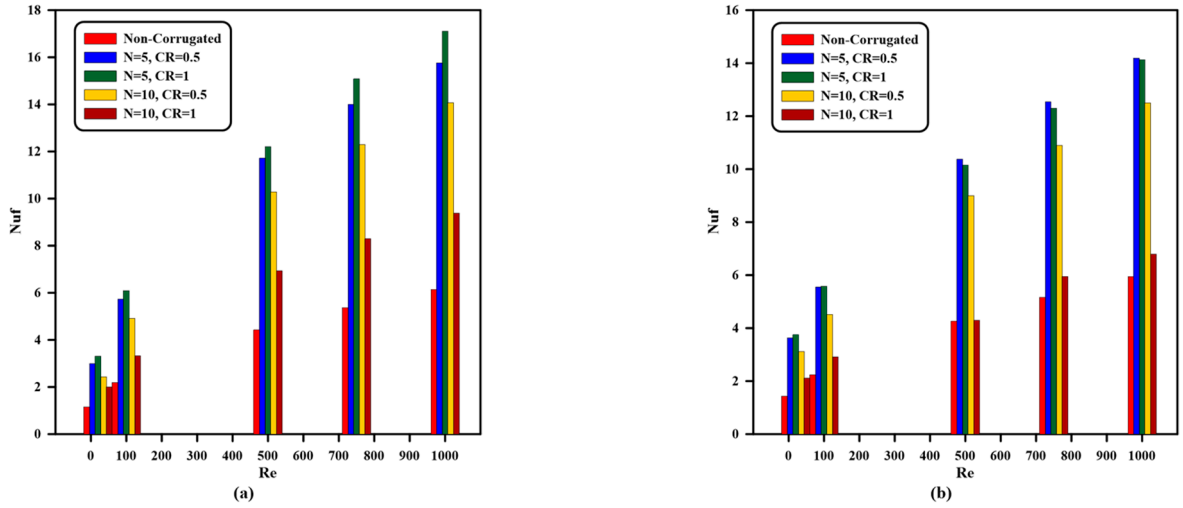


Figure 14. Effect of corrugation on fluid-phase Nusselt number for different values of Reynolds number: (**a**) $D/H = 0.1$; (**b**) $D/H = 0.4$.

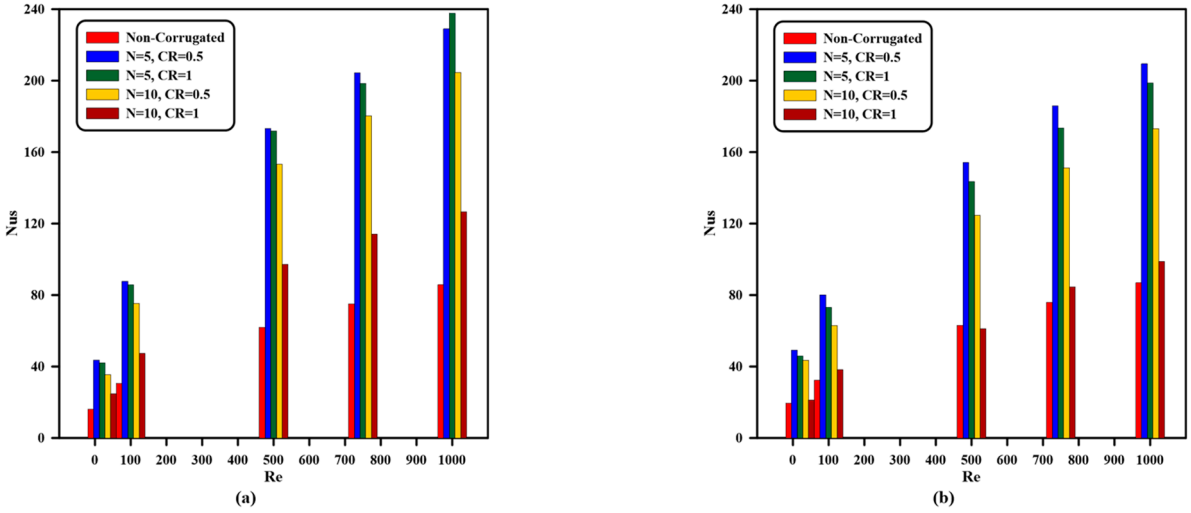


Figure 15. Effect of corrugation on solid-phase Nusselt number for different values of Reynolds number: (**a**) $D/H = 0.1$; (**b**) $D/H = 0.4$.

5. Conclusions

The convection heat transmission inside an L-shaped vented cavity occupied by copper–water nanofluid-saturated copper metal foam with a non-corrugated or corrugated left hot wall was explored numerically. This study determined the outcome of varying different parameters, including the *Re* number, the aspect proportions of the inflow and outflow vent width-to-height length, the solid volume portion of the copper–water nanofluid, and the number of rectangular waves and the corrugation dimension ratio for the corrugated wall case, on temperature and flow fields. According to the results obtained, the following conclusions can be deduced:

- The streamlines intensified and the convection heat flow rose with an increasing Re number and increasing aspect ratios of the inlet and outlet vents, especially when the latter was increased to 0.4;
- The fluid-phase temperature of the metal foam compared to the solid-phase temperature decreased when the volume fraction of the nanofluid particles increased;
- The Nu number for the fluid phase of the copper metal foam near the hot left sidewall increased when the nanoparticle concentration volume ratio increased by 26% at $Re = 1000$ and $D/H = 0.3$, and by 52.9% at $Re = 20$ and $D/H = 0.4$, while the solid-phase Nu number decreased by 11% at $Re = 20$ and $D/H = 0.4$, and by 28% at $Re = 1000$ and $D/H = 0.1$ when the nanoparticle volume fraction increased from 0% to 20%;
- The Nusselt number for the two phases of metal foam greatly intensified with the amplification of the Re number compared with an increase in the inflow and outflow vent aspect ratio; at $\varphi = 20\%$, the fluid-phase Nusselt number rose by 367.56% at $D/H = 0.2$ and by 315.38% at $D/H = 0.4$, whereas the solid-phase Nusselt number increased by 388.28% at $D/H = 0.2$ and by 347.52% at $D/H = 0.4$ when the Reynolds number was augmented from 20 to 1000;
- As the corrugation ratio increased from 0.5 to 1, the penetration of fluid towards the cavity's left sidewall pockets became hard and small re-circulation zones were established within those pockets;
- For the corrugated hot wall, the Nu numbers of the two metal foam phases increased with an increase in the Re number; at $D/H = 0.4$, $\varphi = 10\%$, $N = 5$, and $CR = 0.5$, it was determined that the fluid-phase and solid-phase Nusselt numbers increased by 331.2% and 366.32%, respectively, as the Reynolds number increased in the range of $(20–1000)$;
- For the corrugated hot wall, the Nu number of the two phases decreased with an increase in the aspect ratio; when $Re = 750$, $\varphi = 20\%$, $N = 5$, and $CR = 0.5$, it was determined that the fluid-phase and solid-phase Nusselt numbers decreased by 10.35% and 8.55%, respectively, as the opening aspect ratio increased from 0.1 to 0.4;
- The fluid-phase Nu number near the corrugated left sidewall increased and the solid-phase Nu number decreased with an increase in the nanoparticle volume fraction; the fluid-phase Nusselt number rose by 30% at $Re = 1000$ and $D/H = 0.1$, and by 42% at $Re = 20$ and $D/H = 0.4$, whereas the solid-phase Nusselt number decreased by 9% at $Re = 20$ and $D/H = 0.4$, and by 13% at $Re = 1000$ and $D/H = 0.1$ when the nanoparticle volume fraction was increased from 0% to 20%;
- The fluid- and solid-phase Nusselt numbers for the corrugated wall were higher than those for the non-corrugated wall, irrespective of the number of corrugations or the corrugation ratio;
- By augmenting the corrugation ratio from $CR = 0.5$ to $CR = 1$ at $Re = 500$, $N = 5$, and $D/H = 0.4$, the fluid- and solid-phase Nusselt number values decreased by 13.27% and 19.17%, respectively.
- Increasing the corrugation number from $N = 5$ to $N = 10$ led to a reduction in the Nusselt number value; at $Re = 750$, $CR = 1$, and $D/H = 0.1$, the fluid and solid Nusselt number values decreased by 32.53% and 36.74%, respectively;
- Corrugation is a good option for enhancing thermal performance. For instance, $N = 5$ corrugations and a $CR = 1$ can be utilized to corrugate walls and achieve a high Reynolds number in solar air heaters, solar dryers, green building heating, and electronic cooling in order to achieve a noteworthy heat transfer enhancement without exaggerated flow resistance.

In this contemporary study, a corrugated, L-shaped, vented cavity filled with thermal non-equilibrium nanofluid-saturated metal foam was studied numerically. This study aimed to examine the thermal performance in order to strengthen the practicality of utilizing this system in thermal engineering systems such as solar air heating, heat exchangers, convective drying, etc. There are several limitations that must be considered, as follows: A steady state, incompressibility, and laminar flow were assumed, and the heat transfer rate through radiation and viscous dissipation effects were presumed to be insignificant. Finally, it was assumed that the porous medium was hydrodynamically and thermally isotropic, homogeneous, and saturated with a single-phase nanofluid in a local thermal non-equilibrium with the metal foam's solid phase. In spite of these limitations, the present work supplements our knowledge about the effect of a wide range of relevant parameters on the thermal performance in such enclosures and the effect of wall corrugation on the convection heat transfer inside these enclosures. As no experimental work was performed in the present study, it is recommended to implement this in future work and examine a solar air heating chimney appliance with a corrugated L-shaped vented cavity to enhance the thermal transmission in Baghdad City.

Author Contributions: Conceptualization, L.F.A.; methodology, L.F.A.; software, H.T. and A.M.S.; validation, H.T. and A.M.S.; formal analysis, L.F.A.; investigation, L.F.A.; writing—original draft, L.F.A.; writing—review and editing, H.T. and A.M.S.; supervision, L.F.A., H.T. and A.M.S.; funding acquisition, A.M.S. All authors have read and agreed to the published version of the manuscript.

Funding: This research received no external funding.

Data Availability Statement: Data sharing is not applicable to this article, as no datasets were generated or analyzed during the current study.

Conflicts of Interest: The authors declare no conflicts of interest.

Abbreviations

Latin Symbols

a_{sf}	specific surface area (m^{-1})
C_F	Forchheimer coefficient
C_p	heat capacitance $(J/kg.K)$
D	inlet and outlet vent width (m)
Da	Darcy number
g	acceleration due to gravity (m/s^2)
Gr	Grashof number
h_{sf}	interfacial heat transfer coefficient $(W/m^2.K)$
H	height (m)
k	thermal conductivity $(W/m.K)$
K	permeability (m^2)
L	length (m)
n	normal direction
N	number of corrugation waves
Nu	Nusselt number
p	pressure (Pa)
P	dimensionless pressure
Pr	Prandtl number
Ra	Rayleigh number
Re	Reynolds number
s	coordinate along non-corrugated and corrugated left wall
S	surface length of thermal region (m)
T	temperature (°C)

T_c	cold fluid inlet temperature (°C)
T_h	hot temperature (°C)
u, v	velocity components (m/s)
u_c	cold fluid inlet velocity (m/s)
U, V	dimensionless velocity components
x, y	Cartesian coordinates (m)
X, Y	dimensionless coordinates
Greek Symbols	
α	thermal diffusivity (m^2/s)
β	volumetric thermal expansion coefficient (1/K)
μ	dynamic viscosity (kg/m.s)
ρ	density (kg/m^3)
ε	porosity
φ	nanoparticle volume fraction
θ	dimensionless temperature
Subscripts	
f	water base fluid
nf	nanofluid
np	nanoparticles
s	porous solid matrix

References

1. Saeidi, S.M.; Khodadadi, J.M. Forced Convection in a Square Cavity with Inlet and Outlet Ports. *Int. J. Heat Mass Transf.* **2006**, *49*, 1896–1906. [CrossRef]
2. Mahmoudi, A.H.; Shahi, M.; Talebi, F. Effect of Inlet and Outlet Location on the Mixed Convective Cooling inside the Ventilated Cavity Subjected to an External Nanofluid. *Int. Commun. Heat Mass Transf.* **2010**, *37*, 1158–1173. [CrossRef]
3. Ismael, M.A.; Jasim, H.F. Role of the Fluid-Structure Interaction in Mixed Convection in a Vented Cavity. *Int. J. Mech. Sci.* **2018**, *135*, 190–202. [CrossRef]
4. Abdulwahed, A.S.; Ali, L.F. Numerical Investigation of Natural Convection in a Square Enclosure Partially Filled with Horizontal Layers of a Porous Medium. *Heat Transf.* **2023**, *52*, 874–889. [CrossRef]
5. Alkinani, I.H.; Ali, L.F. Natural Convection in Annulus between Two Concentric Cylinders Partially Filled with Metal Foam Distributed with New Suggested Design. *IOP Conf. Ser. Earth Environ. Sci.* **2022**, *961*, 012032. [CrossRef]
6. Mussa, M.A. Numerical Simulation of Natural Convection in a Rhombic Enclosure with Heated Sidewall Coated with Metal Foam. *Diyala J. Eng. Sci.* **2024**, *17*, 77–90. [CrossRef]
7. Zachi, F.J.; Ali, L.F. Experimental Study of Natural Convection Heat Transfer on an Enclosure Partially Filled Porous Medium Heated from below by Constant Heat Flux. *AIP Conf. Proc.* **2023**, *2651*, 050002. [CrossRef]
8. Mehryan, S.A.M.; Ghalambaz, M.; Chamkha, A.J.; Izadi, M. Numerical Study on Natural Convection of Ag–MgO Hybrid/Water Nanofluid inside a Porous Enclosure: A Local Thermal Non-Equilibrium Model. *Powder Technol.* **2020**, *367*, 443–455. [CrossRef]
9. Ali, L.F.; Humaidi, A.J. Offset Temperature and Amplitude–Frequency Effect on Convection Heat Transfer in Partially Gradient Porous Cavity with Different Outlet Port Locations. *Processes* **2025**, *13*, 2279. [CrossRef]
10. Saidi, M.; Karimi, G. Free Convection Cooling in Modified L-Shape Enclosures Using Copper-Water Nanofluid. *Energy* **2014**, *70*, 251–271. [CrossRef]
11. Saleem, K.B.; Marafie, A.H.; Al-Farhany, K.; Hussam, W.K.; Sheard, G.J. Natural Convection Heat Transfer in a Nanofluid Filled L-Shaped Enclosure with Time-Periodic Temperature Boundary and Magnetic Field. *Alex. Eng. J.* **2023**, *69*, 177–191. [CrossRef]
12. Almeshaal, M.A.; Maatki, C.; Kolsi, L.; Ghachem, K.; Chamkha, A. 3D Rayleigh-Bénard-Type Natural Convection in MWCNT-Nanofluid-Filled L-Shaped Enclosures with Consideration of Aggregation Effect. *Math. Methods Appl. Sci.* **2020**, 1–17. [CrossRef]
13. Jamy, R.H.; Chowdhury, S.; Chowdhury, F.K.; Saha, S. Analyzing Overall Thermal Behaviour of Conjugate MHD Free Convection in L-Shaped Chamber with a Thick Fin. *Case Stud. Therm. Eng.* **2023**, *48*, 103137. [CrossRef]
14. Naseri Nia, S.; Rabiei, F.; Rashidi, M.M.; Kwang, T.M. Lattice Boltzmann Simulation of Natural Convection Heat Transfer of a Nanofluid in a L-Shape Enclosure with a Baffle. *Results Phys.* **2020**, *19*, 103413. [CrossRef]
15. Ma, Y.; Tang, H.; Wang, C. Enhancement of Natural Convection of a Nanofluid by Stress-Free Patches in an L-Shaped Enclosure. *Int. J. Numer. Methods Heat Fluid Flow* **2023**, *33*, 2153–2180. [CrossRef]
16. Massoudi, M.D.; Ben Hamida, M.B. Free Convection and Thermal Radiation of a Nanofluid inside an Inclined L-Shaped Microelectronic Module under the Lorentz Forces' Impact. *Heat Transf.* **2021**, *50*, 2849–2873. [CrossRef]

17. Jain, S.; Bhargava, R.; Gupta, P. Numerical Simulation of Natural Convection MHD Flow in a Wavy L-Shaped Cavity with Line Heat Source Using Hybrid EFGM/FEM. *Heat Transf.* **2022**, *51*, 7030–7055. [CrossRef]
18. Moghimi, S.M.; Domairry, G.; Bararnia, H.; Soleimani, S.; Ghasemi, E. Numerical Study of Natural Convection in an Inclined L-Shaped Porous Enclosure. *Adv. Theor. Appl. Mech.* **2012**, *5*, 237–245.
19. Mojumder, S.; Saha, S.; Rizwanur Rahman, M.; Rahman, M.M.; Rabbi, K.M.; Ibrahim, T.A. Numerical Study on Mixed Convection Heat Transfer in a Porous L-Shaped Cavity. *Eng. Sci. Technol. Int. J.* **2017**, *20*, 272–282. [CrossRef]
20. Sheikholeslami, M.; Rokni, H.B. Numerical Simulation for Impact of Coulomb Force on Nanofluid Heat Transfer in a Porous Enclosure in Presence of Thermal Radiation. *Int. J. Heat Mass Transf.* **2018**, *118*, 823–831. [CrossRef]
21. Moria, H. Natural Convection in an L-Shape Cavity Equipped with Heating Blocks and Porous Layers. *Int. Commun. Heat Mass Transf.* **2021**, *126*, 105375. [CrossRef]
22. Al-Damook, A.; Azzawi, I.D.J. Magnetohydrodynamic Natural Convection of Water in an L-Shaped Container Filled With an Aluminum Metal Foam. *J. Heat Transf.* **2023**, *145*, 022601. [CrossRef]
23. Yeasmin, S.; Billah, M.M.; Molla, M.Z.; Hoque, K.E. Numerical Analysis of Unsteady Mixed Convection Heat Transfer Characteristics of Nanofluids Confined within a Porous Lid-Driven L-Shaped Cavity. *Int. J. Thermofluids* **2022**, *16*, 100218. [CrossRef]
24. Azzawi, I.D.J.; Khalil, W.H.; Al-damook, A. Multiobjective Optimization of Free Convection through a Nonuniform Cabinet Filled with Porous Media. *Heat Transf.* **2023**, *52*, 3300–3316. [CrossRef]
25. Alawee, W.H.; Al-Sumaily, G.F.; Dhahad, H.A.; Thompson, M.C. Numerical Analysis of Non-Darcian Mixed Convection Flows in a Ventilated Enclosure Filled with a Fluid-Saturated Porous Medium. *Therm. Sci. Eng. Prog.* **2021**, *24*, 100922. [CrossRef]
26. Mahmud, S.; Pop, I. Mixed Convection in a Square Vented Enclosure Filled with a Porous Medium. *Int. J. Heat Mass Transf.* **2006**, *49*, 2190–2206. [CrossRef]
27. Bhuiyan, A.A.; Banna, M.H.; Barna, S.F.; Amin, M.R.; Sadrul Islam, A.K.M. Numerical Modelling of Thermal Characteristics in a Microstructure Filled Porous Cavity with Mixed Convection. *Int. J. Heat Mass Transf.* **2016**, *93*, 464–476. [CrossRef]
28. Ali, L.F. Natural and Mixed Convection in Square Vented Enclosure Filled with Metal Foam. *J. Eng.* **2015**, *21*, 60–79. [CrossRef]
29. Shi, Y.S.; Liu, D.; Wang, Y.; Zhao, F.Y.; Li, Y.X. Forced Flow Structure and Mixed Convection in a Ventilated Porous Enclosure with a Local Contaminant Source. *Int. J. Heat Mass Transf.* **2019**, *131*, 973–983. [CrossRef]
30. Ghalambaz, M.; Moattar, F.; Karbassi, A.; Sheremet, M.A.; Pop, I. Triple-Diffusive Mixed Convection in a Porous Open Cavity. *Transp. Porous Media* **2017**, *116*, 473–491. [CrossRef]
31. Behzadi, T.; Shirvan, K.M.; Mirzakhanlari, S.; Sheikhrobat, A.A. Numerical Simulation on Effect of Porous Medium on Mixed Convection Heat Transfer in a Ventilated Square Cavity. *Procedia Eng.* **2015**, *127*, 221–228. [CrossRef]
32. Ghazanfarian, J.; Abbassi, A. Mixed Convection in a Square Cavity Filled with a Porous Medium and Different Exit Port Position. *J. Porous Media* **2007**, *10*, 701–718. [CrossRef]
33. Ataei-Dadavi, I.; Chakkingal, M.; Kenjeres, S.; Kleijn, C.R.; Tummers, M.J. Experiments on Mixed Convection in a Vented Differentially Side-Heated Cavity Filled with a Coarse Porous Medium. *Int. J. Heat Mass Transf.* **2020**, *149*, 119238. [CrossRef]
34. Sheremet, M.A.; Pop, I.; Ishak, A. Double-Diffusive Mixed Convection in a Porous Open Cavity Filled with a Nanofluid Using Buongiorno's Model. *Transp. Porous Media* **2015**, *109*, 131–145. [CrossRef]
35. Sheremet, M.A.; Roşca, N.C.; Roşca, A.V.; Pop, I. Mixed Convection Heat Transfer in a Square Porous Cavity Filled with a Nanofluid with Suction/Injection Effect. *Comput. Math. Appl.* **2018**, *76*, 2665–2677. [CrossRef]
36. Ullah, N.; Nadeem, S.; Saleem, A. Finite Element Analysis of Convective Nanofluid Equipped in Enclosure Having Both Inlet and Outlet Zones. *J. Taiwan Inst. Chem. Eng.* **2020**, *113*, 428–441. [CrossRef]
37. Ahmed, S.E. Caputo Fractional Convective Flow in an Inclined Wavy Vented Cavity Filled with a Porous Medium Using Al2O3-Cu Hybrid Nanofluids. *Int. Commun. Heat Mass Transf.* **2020**, *116*, 104690. [CrossRef]
38. Shirvan, K.M.; Mamourian, M.; Ellahi, R. Numerical Investigation and Optimization of Mixed Convection in Ventilated Square Cavity Filled with Nanofluid of Different Inlet and Outlet Port. *Int. J. Numer. Methods Heat Fluid Flow* **2017**, *27*, 2053–2069. [CrossRef]
39. Bahlaoui, A.; Raji, A.; Hasnaoui, M.; Näimi, M. Mixed Convection in a Nanofluid-Filled Vented Rectangular Cavity: Suction and Injection Heat Performance. *Comput. Therm. Sci.* **2014**, *6*, 129–142. [CrossRef]
40. Kherroubi, S.; Benkahla, Y.K.; Labsi, N.; Ragui, K.; Bensaci, A.; Boutra, A.; Ouyahia, S.E.; Benzema, M. Two- and Three-Dimensional Comparative Study of Heat Transfer and Pressure Drop Characteristics of Nanofluids Flow through a Ventilated Cubic Cavity (Part I: Newtonian Nanofluids). *J. Therm. Anal. Calorim.* **2021**, *144*, 623–646. [CrossRef]
41. Chummar, A.; Harish, R. Numerical Investigation of Forced Convective Heat Transfer of Nanofluids within an Enclosure. *Mater Today Proc.* **2022**, *51*, 1465–1472. [CrossRef]
42. Arroub, I.; Bahlaoui, A.; Belhouideg, S.; Raji, A.; Hasnaoui, M. Combined Effects of Inclination Angle and Imposed Flow on Mixed Convective Cooling Inside a Vented Cavity Crossed by Nanofluids. *Phys. Chem. Res.* **2023**, *11*, 631–642. [CrossRef]

43. Sourtiji, E.; Gorji-Bandpy, M.; Ganji, D.D.; Hosseinizadeh, S.F. Numerical Analysis of Mixed Convection Heat Transfer of Al2O3-Water Nanofluid in a Ventilated Cavity Considering Different Positions of the Outlet Port. *Powder Technol.* **2014**, *262*, 71–81. [CrossRef]
44. Job, V.; Gunakala, S.R.; Rushi Kumar, B.; Sivaraj, R. Effects of Heat-Generating Component Size and Porous Layer Thickness on MHD Mixed Convection Flow of Ag-Water Nanofluid Through an L-Shaped Channel. In *Applications of Fluid Dynamics*; Lecture Notes in Mechanical Engineering; Springer: Berlin/Heidelberg, Germany, 2018; pp. 109–126. [CrossRef]
45. Job, V.M.; Gunakala, S.R. Unsteady Hydromagnetic Mixed Convection Nanofluid Flows through an L-Shaped Channel with a Porous Inner Layer and Heat-Generating Components. *Int. J. Heat Mass Transf.* **2018**, *120*, 970–986. [CrossRef]
46. Armaghani, T.; Rashad, A.M.; Vahidifar, O.; Mishra, S.R.; Chamkha, A.J. Effects of Discrete Heat Source Location on Heat Transfer and Entropy Generation of Nanofluid in an Open Inclined L-Shaped Cavity. *Int. J. Numer. Methods Heat Fluid Flow* **2019**, *29*, 1363–1377. [CrossRef]
47. Armaghani, T.; Ismael, M.A.; Chamkha, A.J.; Pop, I. Mixed Convection and Entropy Generation of an Ag-Water Nanofluid in an Inclined L-Shaped Channel. *Energies* **2019**, *12*, 1150. [CrossRef]
48. Akkurt, N.; Shedd, T.; Memon, A.A.; Usman; Ali, M.R.; Bouye, M. Analysis of the Forced Convection via the Turbulence Transport of the Hybrid Mixture in Three-Dimensional L-Shaped Channel. *Case Stud. Therm. Eng.* **2023**, *41*, 102558. [CrossRef]
49. Kherroubi, S.; Ragui, K.; Labsi, N.; Benkahla, Y.; Boutra, A.; El Ganaoui, M.; Liu, B.; Bennacer, R.; Morsli, S.; Darcherif, M. Three-Dimensional Numerical Study of Mixed Convection within a Ventilated Cavity (Shape 'L') Crossed by a Nanofluid under the Effect of a Magnetic Field. *MATEC Web Conf.* **2020**, *307*, 01027. [CrossRef]
50. Ouri, H.; Selimefendigil, F.; Bouterra, M.; Omri, M.; Alshammari, B.M.; Kolsi, L. MHD Hybrid Nanofluid Convection and Phase Change Process in an L-Shaped Vented Cavity Equipped with an Inner Rotating Cylinder and PCM-Packed Bed System. *Alex. Eng. J.* **2023**, *63*, 563–582. [CrossRef]
51. Nield, D.A.; Bejan, A. *Convection in Porous Media*; Springer International Publishing: Berlin/Heidelberg, Germany, 2017. [CrossRef]
52. Alazmi, B.; Vafai, K. Constant Wall Heat Flux Boundary Conditions in Porous Media under Local Thermal Non-Equilibrium Conditions. *Int. J. Heat Mass Transf.* **2002**, *45*, 3071–3087. [CrossRef]
53. Xu, H.J.; Gong, L.; Zhao, C.Y.; Yang, Y.H.; Xu, Z.G. Analytical Considerations of Local Thermal Non-Equilibrium Conditions for Thermal Transport in Metal Foams. *Int. J. Therm. Sci.* **2015**, *95*, 73–87. [CrossRef]
54. Wang, B.; Hong, Y.; Hou, X.; Xu, Z.; Wang, P.; Fang, X.; Ruan, X. Numerical Configuration Design and Investigation of Heat Transfer Enhancement in Pipes Filled with Gradient Porous Materials. *Energy Convers. Manag.* **2015**, *105*, 206–215. [CrossRef]
55. Ghashim, S.L. A Mathematical Analysis of Nanoparticles on Heat Transfer in a Circular Pipe. *Case Stud. Therm. Eng.* **2021**, *28*, 101524. [CrossRef]
56. Al-Farhany, K.; Abdulsahib, A.D. Study of Mixed Convection in Two Layers of Saturated Porous Medium and Nanofluid with Rotating Circular Cylinder. *Prog. Nucl. Energy* **2021**, *135*, 103723. [CrossRef]

Disclaimer/Publisher's Note: The statements, opinions and data contained in all publications are solely those of the individual author(s) and contributor(s) and not of MDPI and/or the editor(s). MDPI and/or the editor(s) disclaim responsibility for any injury to people or property resulting from any ideas, methods, instructions or products referred to in the content.